Simulative Investigation of Optimal Multiparameterized Cooling Plate Topologies for Different Battery System Configurations

Alexander Epp,* Sunny Rai, Finn van Ginneken, Andreas Varchmin, Jürgen Köhler, and Dirk Uwe Sauer

To design an effective battery thermal management system, multiple simulations with different levels of modeling, physics, and details are generally needed. However, complex and high-resolution models are time-consuming, both in terms of buildup and in computation time. Especially the fast-moving early-stage development phases demand all-in-one model approaches allowing for quick and efficient concept evaluations. To meet these requirements, herein, a lumped-mass modeling approach is proposed and a methodology for evaluating various liquid cooling plate topologies is derived. The framework aims to assist the volatile concept phase of battery system development in providing multidimensionally optimized cooling plate topologies. A novel modeling strategy preselects plate parameters using a reduction procedure that couples the transient models' accuracy with the steady-state models' computation time advantages. The results analyze different initial battery geometries, indicating significant deviations in their optimized cooling plate properties. Plate topologies are varied between their main construction design parameters: tube size and tube-to-tube distance. In addition to battery's mean temperature, further meaningful parameters like resulting volume flow are evaluated, compared, and discussed for the entire set of battery geometries. Subsequent sensitivity analyses show geometry-related optimal plate topologies depending on the cooling circuit performance, stressing the necessity for early-stage cooling plate investigations.

1. Introduction

With increasing climate concerns, especially over the past decade, the world economies came together under the Paris Climate Agreement, which aims to contain environmental pollution by keeping the cap on the rising average temperature of the world below 2 °C.[1,2] According to the International energy agency (IEA),[3,4] road traffic is responsible for ≈15% of global CO_2 emissions. To address this issue, major automobile manufacturers are electrifying their drivetrains to eliminate exhaust emissions.[5–7]

The main component of the electric drivetrain is the high-voltage (HV) battery system. Battery electric vehicles (BEVs) use the electrochemical energy stored in the battery cell as an energy source. Typically lithium-ion batteries (LIBs) are preferred due to high energy densities, durability, wide voltage range, and long cycle life.[8–11] The LIBs are connected in various series and parallel combinations

A. Epp, D. U. Sauer
Chair for Electrochemical Energy Conversion and Storage Systems
Institute for Power Electronics and Electrical Drives (ISEA)
RWTH Aachen University
52074 Aachen, Germany
E-mail: alexander.epp2@volkswagen.de

A. Epp
Technical Development
Volkswagen AG
38436 Wolfsburg, Germany

S. Rai
Pre-Series Development, Concepts and Simulation
Center of Excellence Battery
38112 Braunschweig, Germany

The ORCID identification number(s) for the author(s) of this article can be found under https://doi.org/10.1002/ente.202300405.

S. Rai, F. van Ginneken, J. Köhler
Institut für Thermodynamik (IFT)
Technische Universität Braunschweig
38106 Braunschweig, Germany

F. van Ginneken, A. Varchmin
TLK-Thermo GmbH
38106 Braunschweig, Germany

D. U. Sauer
Helmholtz Institute Münster (HI MS)
IEK 12
Forschungszentrum Jülich
52425 Jülich, Germany

D. U. Sauer
Institute for Power Generation and Storage Systems (PGS)
E.ON ERC
RWTH Aachen University
52074 Aachen, Germany

D. U. Sauer
Jülich Aachen Research Alliance
JARA-Energy
52056 Aachen, Germany

**ADVANCED
SCIENCE NEWS**

www.advancedsciencenews.com

Energy Technology

Generation, Conversion, Storage, Distribution

www.entechnol.de

to achieve the requirements for the battery pack. In recent years, the major roadblock hindering the mass of BEVs has been the slow recharging times, that is, refueling time in comparison to the conventional ICEs.[12,13] For example, if 1 C is referred to as the charging rate required to fully charge the vehicle in 1 h, it can take up to 10 h to completely charge the BEV using a C/10 charging rate with an alternating current (AC) level 2 charger. To minimize this refueling gap, regulatory institutions like the United States Department of Energy and The Batteries European Partnership Association have proposed a fast charging time of below 20 min.[14,15] However, high charging rates generate a large amount of heat which leads to high battery temperatures. If high temperatures are not controlled it will degrade battery performance and possesses certain thermal challenges like short circuit and explosion.[16,17] Therefore, a suitable BTMS is required to keep the battery in an optimal temperature range of 20–40 °C.[18,19]

Lempert et al.[20] and Kumar Thakur et al.[21] explored advanced BTMS for LIBs in BEVs during fast charging. They emphasized the need for effective battery management systems to dissipate heat and highlighted methods such as phase change materials and liquid cooling as promising solutions for future research. Currently, various cooling types have been employed in BTMS such as air cooling,[22,23] liquid cooling,[18,21,24–28] refrigerant cooling,[28,29] heat pipes,[30,31] and phase-change material cooling.[17,32–34] Among these methods, the liquid cooling approach is widely used because of its high specific heat capacity, good thermal conductivity, and low cost.[35,36]

To optimize the design of BTMS, Tang et al.[37] focused on improving the heat dissipation of a lithium battery pack through the implementation of a water cooling strategy combined with minichannels and introduced an optimization technique for the cooling structure. The researchers found that enhancing the performance of the system is achievable by increasing the flow rate of the cooling fluid and reducing the temperature at the inlet. Hopp[26] proposed a thermal management system design for lithium-ion pouch cells in vehicles, along with a simulation method to predict battery temperatures and how they interact with the cooling system. Using existing modeling methods, the author studied the heat generated by the battery by measuring single cells and then applied this information to a simulation model. The results demonstrate the importance of integrating both experimental and simulation tools during development. In a study conducted by E et al.,[38] the impact of various parameters on the cooling effectiveness of a battery thermal management system that utilizes a liquid cooling system was examined. The results showed that the number of pipes greatly impacts the cooling plate's average temperature. On the other hand, both the velocity of the coolant and the number of pipes had a similar effect on temperature consistency. Jarrett and Kim[39] used a numerical optimization algorithm based on three objective functions: pressure drop, temperature uniformity, and average temperature. The optimal designs were found to have wide channels for low average temperature and a narrowing channel design for temperature uniformity. The study showed that the convergence behavior could vary with the initial design and that there were many local optima with equivalent performance. The limitations of the study include a limited design space and restricted boundary conditions.

Li et al.[40] utilized a combination of response surface methodology and a nondominated sorting genetic algorithm for multiobjective optimization of a mini U-channel cooling plate using SiO_2 nanofluid. The Pareto optimal solution provides optimal design variables for maximum temperature, temperature difference, and pressure drop, aiding in the design of BTMS with nanofluids. Zuo et al.[41] designed an improved multichannel cooling plate and analyzed it to enhance its performance. The researchers employed Taguchi experimental design, grey relational analysis, and analysis of variance to investigate the effects of various factors on the performance of the improved cooling plate. The research provides valuable guidance for designing improved multichannel cooling plates and understanding the factors that affect their performance. Zhang et al.[42] proposed an innovative design of an inclined channel cooling plate and compared it with the conventional straight-through design. The inclined channel showed significant improvements in both heat transfer performance and pressure drop reduction. Zuo et al.[43] developed a double S-channel cooling plate specifically designed for cooling a prismatic LiFePO$_4$ battery. A comparative analysis is conducted between the double S-channel cooling plate and a single S-channel cooling plate in terms of maximum temperature, temperature difference, pressure drop, and pumping power. The results demonstrated that the double S-channel cooling plate exhibited significant advantages in terms of the temperature difference and pressure drop, while the maximum temperature was comparable between the two designs. Zuo et al.[35] further investigated double-sided cooling of a prismatic LiMn$_2$O$_4$ battery using mini U-channel cooling plates, emphasizing thermal performance effects depending on the flow direction. Li et al.[36] compared the effects of pulsating flow and steady flow on heat transfer and energy consumption in a multichannel cooling plate for BTMS. The study concluded that the pulsating flow has both positive and negative effects, and optimizing the pulsation frequency and amplitude can minimize energy consumption. Gonzalez-Aguirre et al.[44] focused on cell selection and proposed a methodology that takes into account the thermal and electrical performance, especially for fast charging cases. They provide a thorough approach to cell selection.

Up to the present, various investigations have been carried out on air- and liquid-cooled systems separately using experimental investigations, numerical simulations, and optimization methods. Thakur et al.,[21] Gonzalez-Aguirre et al.,[44] Nikolaos et al.[45] and Lempert et al.[20] investigated the technical challenges associated with fast charging, but there has been limited discussion on the process of designing a battery cooling plate based on the fast charging needs. In order to optimize the battery cooling plate at an early stage of development, this work proposes a lumped mass model for a single-battery module that can be scaled up to a battery pack level. The method is preferred over complex high-resolution topology optimization and parametric studies that are time-consuming and not adjustable to varying boundary conditions and concepts. The cooling channel topology will be optimized using an abstract approach that reduces the topology to the interconnection of multiple tubes. In order to explore the cooling plate design of a selected fast charging capable LIB system, different cooling system configurations are evaluated based on the output from the thermal model, that is, mean temperature (T_{Mean}), maximum temperature (T_{Max}),

and temperature spread (T_{Spread}). For a fast charging profile, temperatures obtained from the thermal model are compared to those obtained from different cooling configurations. Based on that, an optimal cooling configuration in the solution space is recommended.

In this research, the focus is on the design of the optimal cooling topology for different battery pack sizes and provides a novel modeling approach to optimize the cooling plate design using coupled electrothermal simulation models.

Major contributions of this work are 1) deriving a novel multi-parametric cooling plate simulation model for evaluating various cooling plate topologies at concept stages. Thereby, the entire cooling circuit and the corresponding pressure losses are generically parameterized. Thus, the coupled effects in the design of the cooling plate can be evaluated given various battery cooling requirements. 2) Eliminating the use of detailed computer-aided design (CAD) models in the early design process through a multistage cooling plate optimization procedure for various design parameters. 3) Cooling-specific evaluation of different cellmodules geometries with respect to their cooling plate capability based on aggressive fast charging requirements.

The remainder of this study is organized as follows: Section 2 will present a description of the optimization process for the cooling plate, including the modeling approach used. This will be followed by a detailed account of the numerical optimization results of three geometrically different cellmodules in Section 3. The study will then be concluded in Section 4, with an overview of the main findings and a discussion of potential areas for future research. **Figure 1** summarizes the procedure of cooling plate evaluation in this work.

2. Experimental Section

In the following section, the optimization processes for the cooling plate topology and the associated models are presented. Section 2.1 first describes the overall optimization process that is used to narrow down various cooling plate parameters until an optimal set of parameters is identified. Subsequently, Section 2.2 describes the modeling approach for the battery modules and other cooling system components. With these approaches, the models that are used in the respective optimization stage are developed. The following sections focus on modeling heat sources and heat conduction with suiting assumptions for the entire battery from the cell to the module to the system level. Section 2.2.1 describes the heat conduction and the heat sources and Section 2.2.2 describes the modeling of the cooling
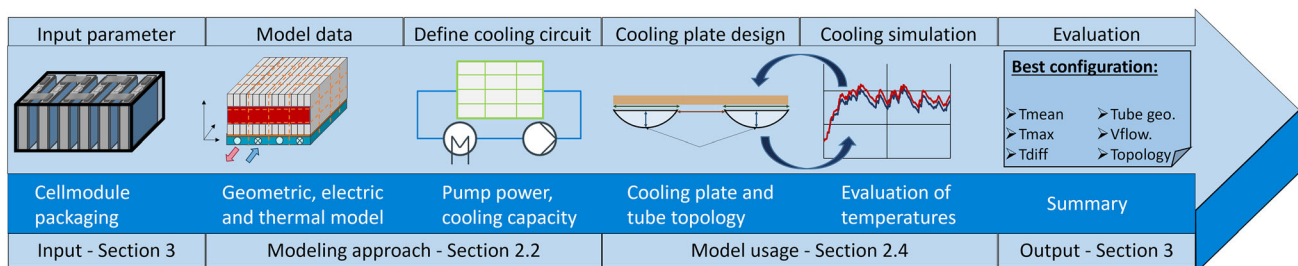
plate, which represents the heat sink. In the following sections, symmetry assumptions (see Section 2.2.3) and the modeling of pressure losses (see Section 2.2.4), as well as other components in the battery system (see Section 2.2.5) are described. Section 2.3 discusses model limitations, and Section 2.4 illustrates model usage.

### 2.1. Optimization Process and Model Input and Output Parameter

In order to determine the requirements for cooling plates, the irreversible heat losses within the battery cells and the heat transfer to the cooling system must be calculated. The irreversible heat losses can be described as a function of power or current using electrical equivalent circuit models (ECMs). ECMs with RC elements are often used to evaluate transient power profiles. However, transient evaluation combined with a large number of variable cooling plate parameters leads to a multidimensional solution space and, thus, to high computation times. A commonly used means of reducing the computational time of simulation models is to omit transient simulations by reproducing them based on appropriate steady-state or quasi-steady-state simulations. While this procedure effectively reduces computational time, it also has some drawbacks. The more the simulation is simplified, the more the model accuracy and corresponding validity of the simulation results may suffer. Therefore, an optimization process flow was developed for this work that uses parameter-specific partial evaluations from the steady-state, quasi-steady-state, or transient simulation and incorporates the partial solution into the rest of the workflow. Depending on the type of simulation, individual parameters are evaluated in the respective stage, while other parameters are not considered at first. Thereby, the advantages of accuracy are combined with those of computing speed. **Figure 2** illustrates the procedure.

On the left side in Figure 2, the inputs of the optimization process are shown. The inputs are adapted according to the model used. Each optimization step in the modeling section, except for the last one, is used to reduce possible cooling plate topologies. With the help of the last step, the parameters found for a topology are verified. Thus, the combinatorics of steady-state and quasi-steady-state models serves to identify optimal cooling plate topologies within the entire solution space.

In order to maintain the highest accuracy of the overall cooling system, the thermal network and the corresponding cooling circuit are calculated transiently in all three models. However, each of the three models is served with a different and

Input parameter	Model data	Define cooling circuit	Cooling plate design	Cooling simulation	Evaluation
					Best configuration: ⟶Tmean ⟶Tube geo. ⟶Tmax ⟶Vflow. ⟶Tdiff ⟶Topology
Cellmodule packaging	Geometric, electric and thermal model	Pump power, cooling capacity	Cooling plate and tube topology	Evaluation of temperatures	Summary
Input - Section 3	Modeling approach - Section 2.2		Model usage - Section 2.4		Output - Section 3

Figure 1. Schematic structure of the cooling plate optimization framework presented in this work.
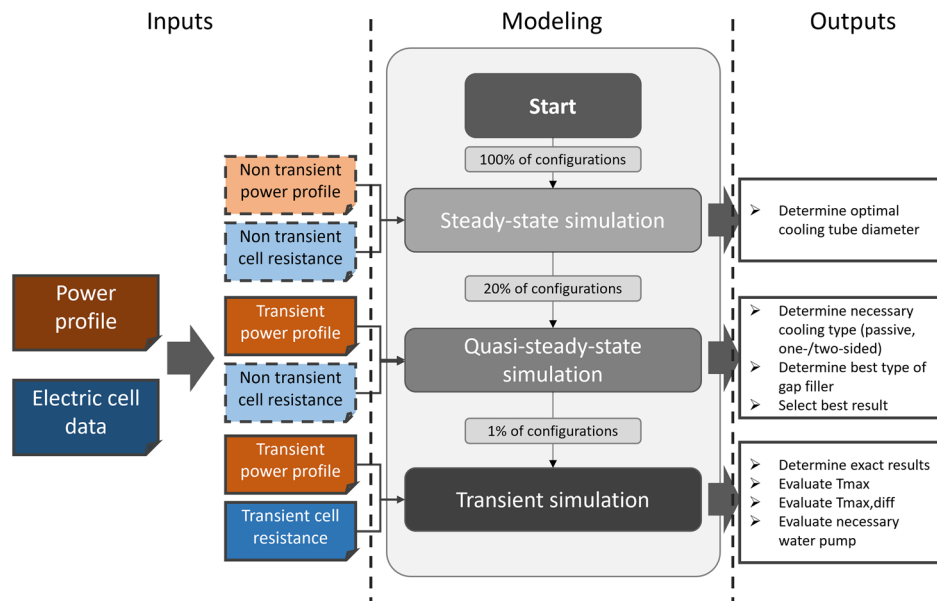
Figure 2. Flowchart diagram of the cooling plate optimization process. Different simulation types (steady-state, quasisteady-state, and transient) are served by type-adjusted inputs for resistance and power. The determined outputs of each stage are based on the type of simulation. The individual simulation stages reduce configurations starting from a large number of cooling plate possible variants.

stage-dependently designed ECM model and power profile. In the first step, the steady-state model with a temperature-dependent voltage source and a temperature-dependent electrical resistance is assumed. This kind of ECM is named Rint-ECM in the following. The state of charge (SOC) is assumed to be constant in the steady-state model. The data for the electrical resistance and the voltage source is provided by the inputs. In addition, the inputs provide a current profile. From this current profile, a squared average c-rate is determined using Equation (2). The c-rate is the ratio between the charging and discharging current and the nominal capacity (Equation (1)). A c-rate of 1 for example means that the battery is charged or discharged within 1 h.

$$c_{\text{Rate}} = \frac{|I|}{C_{\text{cell}}} \tag{1}$$

$$\bar{c}_{\text{Rate}} = \sqrt{\frac{\int_{t_0}^{t_{\text{end}}} c_{\text{Rate}}^2(t) \, \text{d}t}{\text{time}}} \tag{2}$$

The simplifications enable the computation of steady-state temperatures that generally have limited comparability with transient model results. However, a relative comparison between the results of the steady-state models is made possible. Thus, this comparison allows a selection of cooling channel heights, since it can be determined which configuration dissipates the most heat with the smallest possible temperature difference within the cellmodules. Thus, the optimal outcome is identified using the maximum temperature and temperature difference within the module.

The quasi-steady-state also uses a Rint-ECM. However, the dependence of the voltage and the electrical resistance on the SOC is taken into account. Another difference from the steady-state model is that the current profile from the inputs

is used directly. Electrical Rint parameters suitable for the current profile are derived with the transient equivalent circuit model. This allows comparability in terms of ohmic power loss between the quasi-stationary and the transient model. The found electrical parameters are multiplied by a safety factor to ensure that the quasi-stationary model has a slightly higher ohmic power loss than the transient model. The found electrical parameters are also used for the steady-state model. This ensures that the quasisteady-state model does not underestimate temperatures. Generally, to limit the risk of overestimation of the ohmic power losses, this safety factor has to be kept as small as possible. Thereby, the optimization of overly conservative cooling plate design can be prevented.

With the prior knowledge of the optimal cooling channel height, the number of cooling plate topologies is significantly reduced. The remaining cooling plate topologies are calculated using the efficient quasisteady-state model, and the optimal set of parameters is determined.

In the final step of the optimization process, an impedance-based ECM consisting of a voltage source, electrical resistance, and two RC elements (see Appendix) is used to verify the optimal parameter sets from the quasisteady-state model with respect to the cooling system requirements. This type of ECM is called RC-ECM in the following.

The preselection of suitable cooling plate configurations in the proposed optimization process by stationary and quasi-stationary models is essential for a fast evaluation. Preselected configurations are finally evaluated with the transient model to be optimized with respect to the resulting cellmodules temperatures. The optimization process used in this work can be used for the early development phases and thus aims for a conservative evaluation of different cooling plate concepts based on variable inputs. It allows the evaluation and comparison of cooling plate

concepts regarding their general suitability for given battery specifications. General model limitations are discussed in Section 2.3.

2.2. Modeling Approach

The model presented here is based on the work of Wendland et al. in ref. [46]. The cooling plate optimization process presented here is capable of evaluating various cooling plate topologies combining several design parameters and optimizing numerous variable combinations for the entire EV battery system within a few seconds. The simplified, parametrizable base model is composed of interconnected discrete point masses and is used to optimize the cooling plate topology with either indirect/passive air or active liquid cooling. For the modeling of the battery system and its components, Modelica with the MSL (Modelica Standard Library) 4.0.0 is used. Additionally, the base model is built with custom and already implemented models from the TIL library in Modelica.[47,48] The parameterization and validation of the base model are based on various computational fluid dynamics (CFD) simulations for different parts of the whole cooling plate topology. Furthermore, the modeling of the battery cells and the cooling plate was validated with a reference cellmodules by Wendland.[49] The reference module consisted of 24 pouch-shaped battery cells oriented parallel to the fluid flow in the cooling plate. The test was performed in an air-conditioned test chamber. In addition, the reference module was insulated on the noncooled surfaces to minimize the influence of the environment. Current pulses with a duration of 30 s were used to achieve steady-state temperatures. In summary, simulation and measurement showed very small deviations regarding the temperature, the overall temperature level of the cells was well represented, and the modeling was successfully validated. A detailed description of the validation process can be found in the work from Wendland.[49]

The proposed model can evaluate the entire heat path from the generation of heat in the LIB module through heat transport into the coolant to heat exchange in the chiller. Thereby, an almost entirely parameterizable approach was chosen. The assumed battery module can represent different cell sizes, chemistries, and cell-level interconnections. Dependencies are evaluated geometrically, electrically, and thermally by the cooling model. A heat transfer path from the module into the cooling plate was described using known equations. A distinction can be made between passive air cooling, one-sided, and two-sided water/glycol cooling. Different gap filler thicknesses and types can be selected explicitly in an internal optimization for the necessary heat transfer. Different geometries of the cooling channels can be easily parameterized via the cross-sectional area and the perimeter. In addition, the number of passes (U/W-connections) can be parameterized. Pressure losses are calculated using multiple subdivisions inside and outside the cooling plate. Thus, a pump capacity is derived using the necessary water/glycol flow rate calculated for an optimum cooling capability in the specific cooling plate configuration. Different dimensioning of the cooling circuit reflects different cooling capacities and thus directly influences the overall optimized result of the cooling plate configuration. The following section describes the individual parts

and modeling approaches of the overall cooling plate optimization framework.

2.2.1. Modeling of the Cell, Module, and Battery System

The objective of modeling the battery system is to describe the individual cellmodules and fluid flow in the cooling plate sufficiently accurately and efficiently in terms of thermal behavior. Therefore, it is necessary to make abstractions for the model development.

The first abstraction comprises the battery system. The battery system is considered as a hydraulic and electrical interconnection of multiple cellmodules. Other components like the E-Box are not considered. The second abstraction involves the module itself. It is considered as a homogeneous block with an anisotropic thermal conductivity in three spatial directions. According to Wendland,[49] this abstraction admits that the temperature spread can be underestimated if contact resistances and insulation layers are neglected. Under the condition that the heat conduction path toward cooling is calculated correctly, the maximum temperature in the range $< 60\,°C$ is represented sufficiently accurately. The third abstraction concerns the discretization. The discretization of a module depends on the discretization of the cooling channels and the cooling coils (see Section 2.2.2). Through this approach of discretization, individual cells in the module are not resolved and a discrete point mass can contain a part of a cell or several cells, depending on the discretization, it should be noted that the discretization in the height of the module can be freely chosen. Consequently, the module is modeled as a thermal network consisting of discrete point masses with a temperature state in the center (see **Figure 3**) and anisotropic heat transfers. For model development, it is also assumed that convective heat transfer with a constant coefficient to air exists on the side surfaces of the module. The cooling plate is always located on the bottom side of the module. Double-sided cooling is made possible by a symmetry plane in the height of the module.

There are two types of discrete elements in the model. Type 1 includes 1D transient heat conduction equation and is used to model the busbar system (consisting of tabs and busbars). Type 2 is used to model the module itself. This type includes the 3D transient heat conduction equation.[50] Thus, the anisotropic thermal conductivity of the active material of the battery cells can be considered. The elements of the Type 2 include not only the active material of the individual cells in the module but also all other installed materials and components in the module, for example, the battery module housing (see **Figure 4**).

As shown in Figure 4, the module is discretized in three dimensions. The number of elements in length is denoted by the index i, those in width by the index j, and those in height by the index k. The heat flow rate $\dot{Q}_{i,j,k,\text{surface}}$ over the respective surface (see Figure 3) of each element can be determined as follows

$$\dot{Q}_{i,j,k,\text{surface}} = \frac{T_{i,j,k,\text{surface}} - T_{i,j,k}}{R_{\text{th},i,j,k,\text{surface to center}}}$$

$$\text{surface} \in [\text{North, South, West, East, Front, Back}]$$

(3)
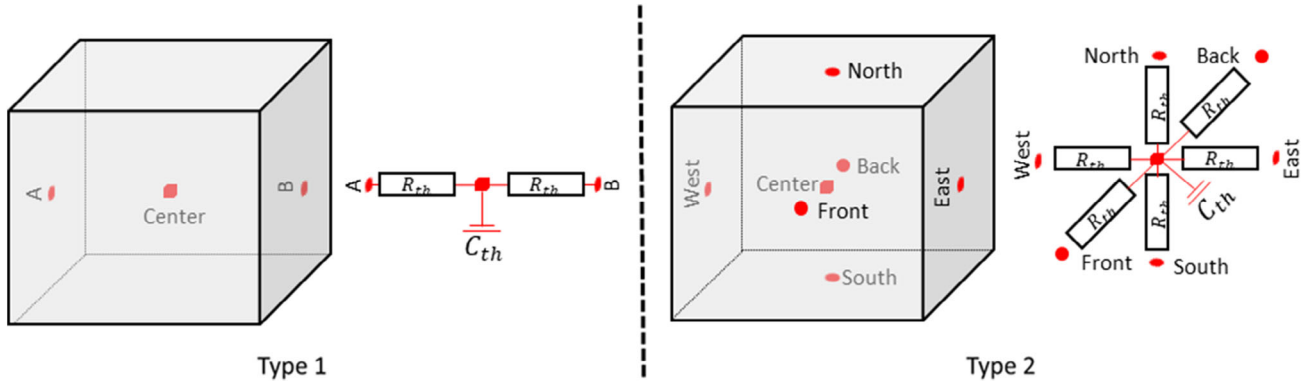
Figure 3. Schematic illustration of a discrete element divided into Type 1 and Type 2 elements. The thermal equivalent circuit is shown to the right of the respective element.
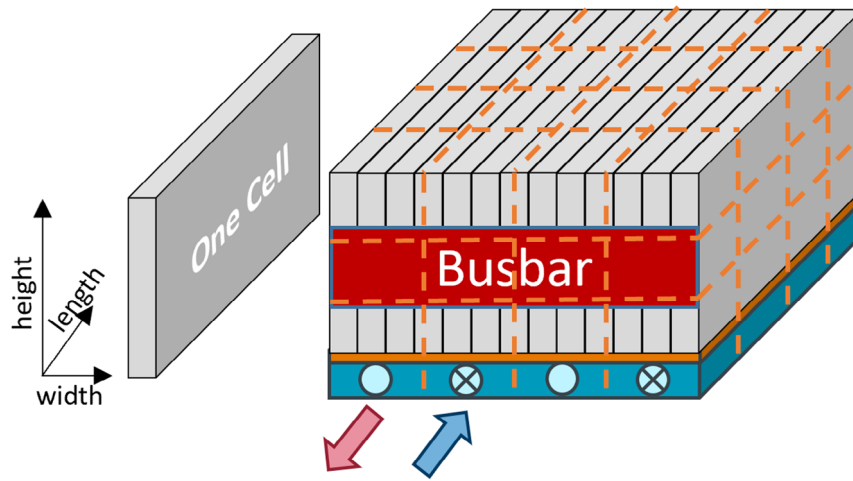
Figure 4. Schematic structure of the cellmodules.

The thermal resistance $R_{\text{th},i,j,k,\text{ surface to center}}$ between the respective surface and the center is determined by the geometry and thermal properties of each element representing the 3D thermal resistance of the discrete element. The temperature state of each element can be determined with the help of the first law of thermodynamics and the resulting heat conduction equation as follows[50]

$$
\begin{aligned}
& c_{\text{p, heat module}} \cdot V_{i,j,k} \cdot \rho_{\text{module}} \cdot \frac{dT_{i,j,\,k}}{dt} \\
& = \sum_{\text{surface}} \dot{Q}_{i,j,k,\text{ surface}} + \dot{Q}_{i,j,k,\text{source}}
\end{aligned}
\tag{4}
$$

Thermal conductivities, specific heat capacities, and densities which directly depend on the individual module setup massively determine the thermal behavior of the module. The specific heat capacity is determined on the module level using the cell-specific heat capacity $c_{\text{p,heatcell}}$ and the number of cells n_{cells} for each module. Additionally, packaging materials are added. Therefore, the module heat capacity $c_{\text{p,heatmodule}}$ is defined as

$$
c_{\text{p, heat module}} = \frac{c_{\text{p, heat cell}} \cdot n_{\text{cells}} \cdot m_{\text{cell}} + \sum_{i \in M} m_i \cdot c_{\text{p},i}}{m_{\text{total}}}
\tag{5}
$$

with M being different materials with weight m_i and specific heat capacity $c_{\text{p},i}$ within the battery module. Consequently, the anisotropic thermal conductivity at the module level is also determined considering different materials M as well as the specific module topology. The same applies to the determination of the module density ρ_{module}.

For the calculation of the electrical resistance in each individual discrete element (see Figure 4 gray area), it is assumed that the resistance in one Type 2 element is equal to the electrical module resistance (see Equation (6)). This assumption results from the different proportions of the discrete elements in the active material of the individual cells. Again, it should be noted that a discrete element can have shares in the active material of several cells in the module. Thus, the module's electrical resistance $R_{\text{module}}(T, \text{SOC})$ can be determined as follows

$$
R_{\text{module}}(T, \text{SOC}) = k_{\text{scaled}} \cdot \frac{n_{\text{series}} \cdot R_{\text{cell}}(T, \text{SOC})}{n_{\text{parallel}}}
\tag{6}
$$

ADVANCED
SCIENCE NEWS

www.advancedsciencenews.com

Energy Technology
Generation, Conversion, Storage, Distribution

www.entechnol.de

The scaling factor k_{scaled} can be used to match the electrical resistance to other battery cells without affecting the influence of the temperature and state-of-charge-dependent resistance field. k_{scaled} is the ratio of the electrical cell resistance to a given resistance at a specific SOC and temperature. For known electrical cell data the factor equals 1.

The current in each discrete element is equal to the module current I_{module}, so the irreversible heat for the steady-state and quasisteady-state (see Figure 2) can be determined as follows.

$$\dot{Q}_{source, module} = R_{module}(T, SOC) \cdot I_{module}^2 \quad (7)$$

For the RC-ECM the irreversible heat is calculated from the ohmic losses via the internal resistance R_0, the first RC element $R_{RC,1}$, and the second RC element $R_{RC,2}$. Thus, the irreversible heat is described as follows

$$\dot{Q}_{source, module} = R_{0, module}(T, SOC) \cdot I_{module}^2 \\ + \frac{U_{RC1}^2}{R_{RC,1, module}(T, SOC)} + \frac{U_{RC2}^2}{R_{RC,2, module}(T, SOC)} \quad (8)$$

$U_{RC,1}$ and $U_{RC,2}$ describe the voltage in the respective RC element. The voltage depends on the charge of the capacitance and can be described as follows

$$\frac{dU_{RC,i}}{dt} = \frac{I_{module}^2}{C_{RC,i(T,SOC)}} - \frac{U_{RC,i}}{R_{RC,i}(T, SOC) \cdot C_{RC,i}(T, SOC)} \quad (9)$$

The resistances $(R_{RC,0}(T, SOC)$, $R_{RC,1}(T, SOC)$, and $R_{RC,2}(T, SOC))$ are determined as in the steady-state case using Equation (6). The capacitance $C_{RC,i}(T, SOC)$ of the respective RC element is determined with the help of the time constant $\tau_{RC,i}(T, SOC)$ and the resistance $R_{RC,i}(T, SOC)$. This ensures that the correction factor k_{scaled} is also considered in the capacitance.

Since each discrete element represents only a portion of the module, the irreversible heat $\dot{Q}_{source,module}$ is divided by the number of discrete elements $n_{x,y,z}$, resulting in the following irreversible heat for each discrete element $\dot{Q}_{i,j,k,source}$

$$\dot{Q}_{i,j,k,source} = \frac{\dot{Q}_{source, module}}{n_{length} \cdot n_{height} \cdot n_{width}} \quad (10)$$

Besides the irreversible heat in the Type 2 elements, that of the busbar system (see Figure 4 red area) plays a crucial role for edge elements. The busbar system has 2D discretization with size $n_{width} \cdot n_{height}$. On the front and rear sides of the module, one side of the Type 1 elements representing the busbar system is thermally connected to all Type 2 edge elements of the module. On the other side, the Type 1 elements are thermally connected to the environment.

For the busbar system, three heat sources are considered by ohmic resistances: the electrical contact resistance between the tab and the busbar $\dot{Q}_{Tab,Busbar}$, the irreversible heat in the tabs $\dot{Q}_{Tab}$, and that in the busbar itself $(\dot{Q}_{Busbar})$. The heat sources are determined for each discrete element (index: j, k), as follows

$$\dot{Q}_{j,k,Tab,Busbar} = f_{j,k,distribution} \cdot R_{Tab,Busbar} \cdot I_{module}^2 \cdot n_{Tab,Busbar} \quad (11)$$

$$\dot{Q}_{j,k,Tab} = f_{j,k,distribution} \cdot R_{Tab} \cdot \left(\frac{I_{module}}{n_{parallel}}\right)^2 \cdot n_{Tabs} \quad (12)$$

$$\dot{Q}_{j,k,Busbar} = f_{j,k,distribution} \cdot R_{Busbar} \cdot I_{module}^2 \cdot n_{Busbars} \quad (13)$$

In order to provide a local resolution of the heat contribution through the busbar system and for the scaling of the heat sources, a distribution matrix $f_{distribution}$ is introduced. This matrix has the dimension $n_{width} \times n_{height}$. The matrix entries zeros represent the areas of the module, which are not covered by the busbar system after parameterization. The remaining entries are determined by the area covered by the tabs in each discrete Type 2 element (see Figure 4). The sum of the matrix must be 1 so that the complete busbar system is represented. With the geometric properties of the busbar system and the discretization (defined by the cooling plate, see Section 2.2.2), the mass of each discrete Type 1 element can be determined. The electrical resistances (R_{Tab}, R_{Busbar}) are determined based on the geometry and the electrical conductivity of copper and aluminum. The electrical contact resistance $R_{Tab,Busbar}$ is a settable parameter.

In addition to the heat sources in the busbar system, the heat flows across the balance volume of the busbar system must be determined. For this purpose, the thermal resistance R_{th} of the Type 1 element is determined based on the parameterized busbar system and the material properties. Thus, the heat flow rate to the Type 2 elements (index: type 2) and that to the environment (index: ambient) can be determined as follows

$$\dot{Q}_{i,j,type\,2} = \frac{T_{i,j, active\, surface} - T_{i,j}}{0.5 \cdot R_{th} \cdot f_{i,j,distribution}} \quad (14)$$

$$\dot{Q}_{i,j,ambient} = \frac{T_{i,j,ambient} - T_{i,j}}{0.5 \cdot R_{th} \cdot f_{i,j,distribution}} \quad (15)$$

The temperature $T_{i,j}$ of the respective element in the busbar system is determined as follows

$$f_{i,j,distribution} \cdot m_{module} \cdot c_{p,\, heat\, module} \cdot \frac{dT_{i,j,}}{dt} \\ = \dot{Q}_{i,j,type\,2} + \dot{Q}_{i,j,ambient} + \dot{Q}_{i,j,Tab,Busbar} + \dot{Q}_{i,j,Tab} + \dot{Q}_{i,j,Busbar} \quad (16)$$

The influence of the environment is also considered. Convective heat transfer is assumed on all sides of the module except for the bottom and top in the case of double-sided cooling. The convective heat transfer is modeled using a heat transfer coefficient α. Different heat transfer coefficients can be found in ref. [51–53]. For passive air cooling, the coefficient is vehicle type independent approximated as $\alpha = 5\,W/m^2 K$. This assumption may be further specified in future work. In the following, the modeling of the cooling plate, including the gap filler, is described.

2.2.2. Modeling of the Cooling Plate

The cooling plate geometry is crucial for the discretization of the module (see Figure 4). The number of cooling channels in one coil (see Figure 6) determines the discretization of the module

2300405 (7 of 23)

width. Furthermore, the number of serial cooling channels in a coil determines the fluid paths. For example, two serial cooling channels in one coil result in a U-shaped fluid path, while three channels result in an S-shaped fluid path. The discretization is freely selectable along the cooling channels (in flow direction). The same applies to height discretization. The modeled cooling plate consists of the cooling channels and the gap filler (see **Figure 5**). The gap filler is modeled by thermal resistance. Here, the mass and, thus, the thermal capacity are neglected due to the small thickness of the gap filler ($\approx$1 mm).

The cooling channels are parameterized using the length of the module and the height of the cooling channel, which results in a hydraulic cross-sectional area and a heat transfer area using the assumption of a circular segment and a height-to-width ratio (see Figure 5). The parameterization is done for each discrete element along the flow direction. Thereby several parallel cooling channels can be taken into account. For the calculation of the heat transfer coefficients between the fluid and tube wall as well as the pressure drop in the tubes, a 0D/1D approach is used for each discrete element in the tube. Rotating the cooling plate allows a fluid flow perpendicular to cell orientation. It should be noted that the discretization of the module length is then given by the topology of the cooling plate. A symmetry plane is used for double-sided cooling, assuming the same cooling mass flows and cooling plate geometry. Thus, the following cooling configurations can be investigated: 1) parallel: one sided | perpendicular: one sided; and 2) parallel: double sided | perpendicular: double sided.

The cooling tubes are assumed as circular segments (see Figure 5). A similar shape is also described in ref. [54] for cooling battery cells. An advantage of this form of cooling channels is the noncutting and flexible production of the cooling plates. This work's assumed cooling plates consist of two parts. The cooling channels are formed in the lower part by deep drawing or cold extrusion. The cooling channels are then sealed with the upper part by roll seam welding or pressure welding, for example.[54]

The thermal capacity of the cooling plate is neglected. The distance from a module's border to the first tube is half of the tube-to-tube distance. The distance is used to determine the maximum number of cooling channels. It should be noted that the tube-to-tube distance only affects the maximum number of cooling channels but not the local change of heat sinks.

One goal in the modeling of the cooling plate is to consider different cooling channel geometries and to represent them sufficiently accurately. Equation (18) and (21) are valid for circular channels.[50] Nevertheless, to allow the mapping from the assumed cooling channel geometry (see Figure 5), which differs from the circular geometry, the hydraulic diameter is used. The use of the hydraulic diameter can lead to deviations in some cases, for example, laminar flow or geometries that deviate from the circular shape.[55] For this reason, the model with this particular cooling channel geometry was verified with CFD simulations for pressure losses and heat transfer coefficient. It should be noted that deviations may occur for other cooling channel geometries. Therefore, the applicability of Equation (18) and (21) should be reviewed for deviating cooling channel geometries.

The convective heat transfer for active liquid cooling within the system can be described using the Nusselt number Nu for laminar and turbulent flows

$$\alpha = k_{passive} \frac{Nu \cdot \lambda}{L}$$
$$k_{passive} = \begin{cases} 1 \text{ for active cooling} \\ 0 \text{ for passive cooling} \end{cases} \tag{17}$$

with α as the heat transfer coefficient, which describes the convective heat transfer between wall and fluid, λ the thermal conductivity of the fluid, and L the dimension governing the flow, which corresponds to the hydraulic cooling tube diameter d_h. For passive air cooling, heat transfer is prevented with the help of the parameter $k_{passive}$ so that the heat can only be dissipated via the other surfaces cooled by the environment. In order to find suitable values for the convective heat transfer coefficient α for active liquid cooling, different equations for Nu depending on the fluid and the type of flow are considered.

For laminar flows (Re < 2300), the laminar Nusselt number Nu_{lam} is modeled by the following equations from Baehr et al.[50]

$$Nu_{lam} = \frac{3.657}{\tanh(2.264 \cdot [X^+]^{\frac{1}{3}} + 1.7 \cdot [X^+]^{\frac{2}{3}})} + \frac{0.0499}{X^+} \cdot \tanh(X^+) \tag{18}$$

The dimensionless length X^+ is defined by the following equation. It results from tube length l, hydraulic diameter d_h, as well as the Péclet number Pe. The Péclet number is the product of Reynolds Re and Prandtl Pr number.[50]

$$X^+ = \frac{l}{d_h \cdot Pe} = \frac{l}{d_h \cdot Re \cdot Pr} \tag{19}$$

The Reynolds number Re in each discrete tube element is determined by Equation (20). The substance-specific quantities,
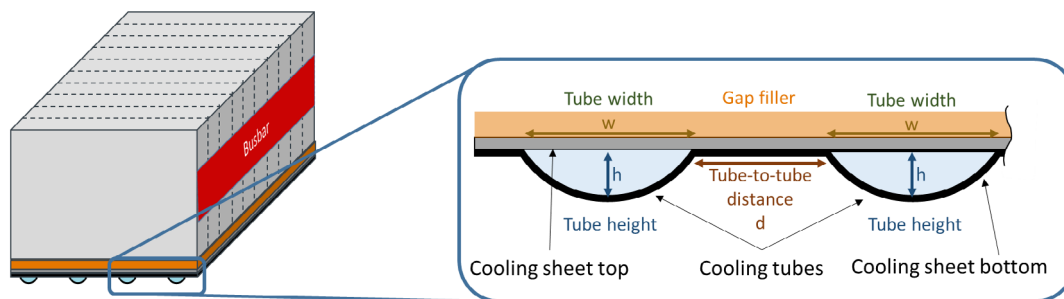
Figure 5. Schematic representation of the cooling plate with multiple geometric design parameters.

2300405 (8 of 23)

ADVANCED
SCIENCE NEWS
www.advancedsciencenews.com

Energy Technology
Generation, Conversion, Storage, Distribution
www.entechnol.de

such as the density ρ_{fluid} and the dynamic viscosity η_{fluid}, are calculated by TIL-Media[47,48] for the incompressible fluid G12Evo. The fluid mass flow in each discrete tube element is determined using the fluid routing and partitioning. Together with the fluid density ρ_{fluid}, the respective volume flow for the tube element is given. Flow velocity v_{fluid} is calculated using the volume flow in each tube element and the respective cross-sectional area.

$$\text{Re} = \frac{\rho_{\text{fluid}} \cdot v_{\text{fluid}} \cdot d_{\text{h}}}{\eta_{\text{fluid}}} \tag{20}$$

For fully turbulent flows ($\text{Re} > 10\,000$), the following equations from Gnielinski[56] are used in the model to calculate the turbulent Nusselt number Nu_{turb}

$$\text{Nu}_{\text{turb}} = \frac{\left(\frac{\xi_{\text{turb}}}{8}\right)\text{Re} \cdot \text{Pr}}{1 + 12.7 \cdot \sqrt{\frac{\xi_{\text{turb}}}{8}} \cdot \left(\text{Pr}^{\frac{2}{3}} - 1\right)} + \left[1 + \left(\frac{d_{\text{h}}}{l}\right)^{\frac{2}{3}}\right] \tag{21}$$

The wall friction coefficient ξ can be described for the turbulent region using the following equation of Konakov (often also named Konakov equation).[57,58]

$$\xi_{\text{turb}} = (1.8 \cdot \log(\text{Re}) - 1.5)^{-2} \tag{22}$$

For the transition region ($2300 < \text{Re} < 10\,000$), linear interpolation is applied between the turbulent and laminar Nusselt numbers. The interpolation is done using the intermittency factor.[59]

2.2.3. Use of Symmetry

An elementary part of the models is the use of symmetries. As already mentioned in Section 2.2.2, a symmetry in height is assumed for the double-sided cooling. This also guarantees the computational performance of the models for this cooling configuration. The discretization of the module width (see Figure 4) is based on the cooling channel passes (n_pass) of one coil in the module (see **Figure 6**). Figure 6 shows the second assumption regarding symmetry. Here the module is reduced to a coil assuming a symmetrical cooling plate. Adiabatic boundaries are assumed at the symmetry surfaces. This means that the surfaces where convection is present must also be scaled. The scaling factor results from the number of coils. With this approach, the computation time can be reduced considerably and allows a wider range of degrees of freedom for the optimization while keeping computation time low. The parameter for the number of passes can be used additionally to increase the degree of freedom in the cooling plate configuration. Depending on the topology, the pipe section at the end of each pass is connected to the next pass's pipe section or the cooling plate's outlet. By this procedure, every second pass flows in the opposite direction to the first.

2.2.4. Modeling of the Pressure Losses

Sufficient flow in the cooling channels, resulting from the pressure drop in the system and the pump, ensures that the cooling plate operates appropriately. A water pump in the circuit must
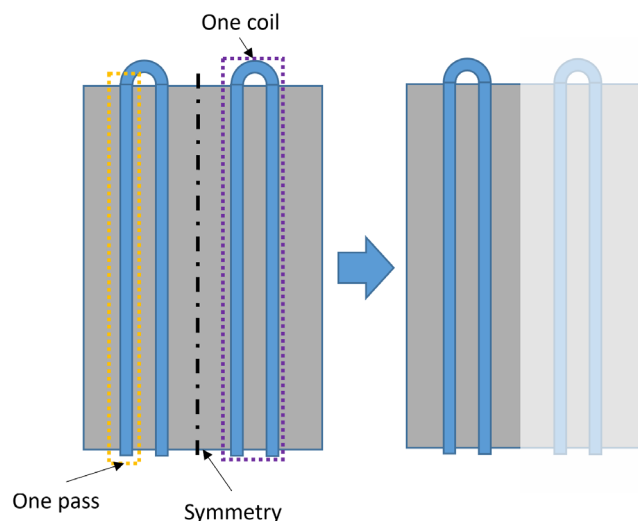

Figure 6. Schematic representation of the symmetry assumption used in the cooling plate optimization model.

therefore be dimensioned to compensate for occurring pressure losses inside and outside of the cooling plate.

Pressure losses inside and outside the cooling plate depend on various parameters like the cooling tube geometry as well as topology, the coolant temperature, and the volume flow rate. However, the overall objective of the pump design is to keep the difference between the inlet and outlet temperatures of the cooling water/glycol mixture relatively small. A homogeneous cooling of the cellmodules can only be achieved by a small difference within the coolant temperatures. This work uses a coolant temperature difference between the inlet and outlet temperature of 5 K as a benchmark.

Pressure loss calculation is divided into multiple parts within the model. **Figure 7** schematically divides the cooling system into different parts and depicts the differently evaluated pressure losses.

In the Tubes: Pressure drops within the tube's straight parts (see (1) in Figure 7) are determined by the following Darcy–Weisbach equation
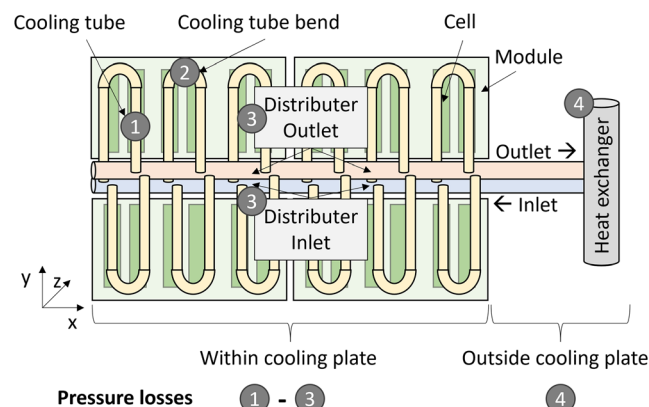
Figure 7. Overview and segmentation of different pressure losses within the entire battery cooling system.

$$\Delta p = \xi \cdot \frac{\rho}{2} v^2 \cdot \frac{l}{d_\mathrm{h}} \tag{23}$$

The pressure drop depends on velocity (v), fluids density (ρ), and wall friction coefficient ξ. The calculation of the wall friction coefficient ξ depends on the Reynolds number. For laminar flows, the Hagen–Poiseuille equation[56] is used

$$\xi_\mathrm{lam} = \frac{64}{Re} \tag{24}$$

For turbulent flows, the wall friction coefficient ξ_turb from Konakov[57,58] is used (see Equation (22)). For the transition region ($2300 < \mathrm{Re} < 10\,000$), linear interpolation is applied as described in Section 2.2.2.

Tube Bends and Distributor of Cooling Fluid: Further pressure drops for cooling tube bends (see (2) in Figure 7) and the distribution of coolant into and from the tubes (see (3) in Figure 7) use an empirical approach with the form of

$$\frac{\Delta p}{\Delta p_\mathrm{nominal}} = \left(\frac{\eta}{\eta_\mathrm{nominal}}\right)^x \left(\frac{\dot{m}}{\dot{m}_\mathrm{nominal}}\right)^y \tag{25}$$

Coefficients are evaluated and validated using various CFD simulation results of a cooling plate substitution model. η_nominal describes the reference coolant dynamic viscosity of the reference simulation. The parameter $\dot{m}_\mathrm{nominal}$ is the reference mass flow rate.

In order to describe the pressure losses in the individual variables, suitable variable sizes for the exponents x and y were then evaluated. The used coefficients for the different components are listed in the following **Table 1**

Outside the Cooling Plate: Pressure losses outside the cooling plate (see (4) in Figure 7) are caused by other operating components necessary for cooling the coolant, such as the chiller, valves, and the associated tubing. These pressure losses are strongly dependent on the individual components as well as their topology and can, therefore, only be accurately calculated in dedicated pressure models. This article, therefore, uses an exemplary dependence for the pressure losses outside the cooling plate to generally describe its dependence on coolant temperature and volume flow rate. The pressure loss assumptions are shown graphically in **Figure 8**.

Table 1. Used coefficients for the empirical approach to calculate the different pressure drops of the components.

Component	$\Delta p_\mathrm{nominal}$ [mbar]	η_nominal [Pa s]	$\dot{m}_\mathrm{nominal}$ [kg s^{-1}]	x	y
Single cooling tube bend	8.15	0.0044	0.026	0.5	1.45
Distribution of inlet & outlet for one-sided cooling	53.45	0.0044	0.31	0.3	1.6
Distribution of the coolant for double-sided cooling	79.84	0.0044	0.63	0.3	1.6

2.2.5. Modeling of the Chiller, Heat Exchanger, and Pump control

As one of the last steps, the heat of the coolant must be dissipated. A simplified chiller stage model is assumed for this purpose. The maximum cooling capacity $\dot{Q}_\mathrm{cooling,max}$ is defined based on three chiller expansion stages using a linear dependence on volume flow (k_V) and fluid temperature (k_T) as well as a cooling capacity offset $\dot{Q}_0$, as follows

$$\dot{Q}_\mathrm{cooling,max} = \dot{Q}_0 + k_\mathrm{V} \cdot \dot{V}_\mathrm{flow} + k_\mathrm{T} \cdot T_\mathrm{fluid,in} \tag{26}$$

The simplified approach allows a fast and sufficiently accurate mapping of the maximum transferable heat for a constant refrigerant inlet temperature of the chiller in the primary cooling circuit. The constants k_V and k_T allow a simplified consideration of the dependencies between maximum transferable heat, volume flow, and coolant inlet temperature in the battery-side coolant cooling $T_\mathrm{fluid,in}$.

The maximum cooling capacity depends on the chiller configuration (see **Figure 9**) and can easily be extended to other configurations. This simplification is used as it can depict a parameterizable cooling capacity with sufficient accuracy while still maintaining a short calculation time of the overall cooling plate optimization model.

Depending on the charge/discharge profile and ambient temperature, a different constant inlet temperature $T_\mathrm{fluid,out,req}$ of the cooling plate can be specified. For driving and charging profiles, the target inlet temperature is set to 20 °C. This applies at an ambient temperature of 20 °C. At 40 °C, the inlet temperature is set to 15 °C. In between, linear interpolation is applied. Outside, a constant extrapolation is applied. Thus, the required heat $\dot{Q}_\mathrm{cooling,req}$ can be determined as follows

$$\dot{Q}_\mathrm{cooling,req} = \dot{m}_\mathrm{fluid} \cdot c_\mathrm{p}(T) \cdot (T_\mathrm{fluid,in} - T_\mathrm{fluid,out,req}) \tag{27}$$

In the case where the heat to be transferred is higher than the maximum cooling capacity, the maximum cooling capacity is used. Consequently, the inlet temperature can be determined with the following equation
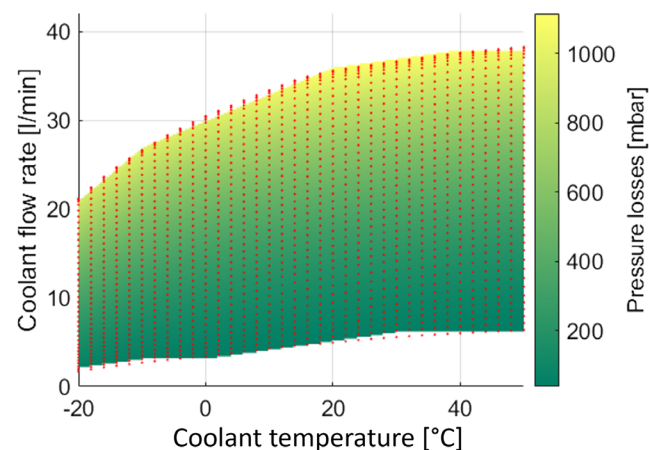
Figure 8. Data-based pressure losses outside of the cooling plate depending on volume flow rate and coolant temperature.
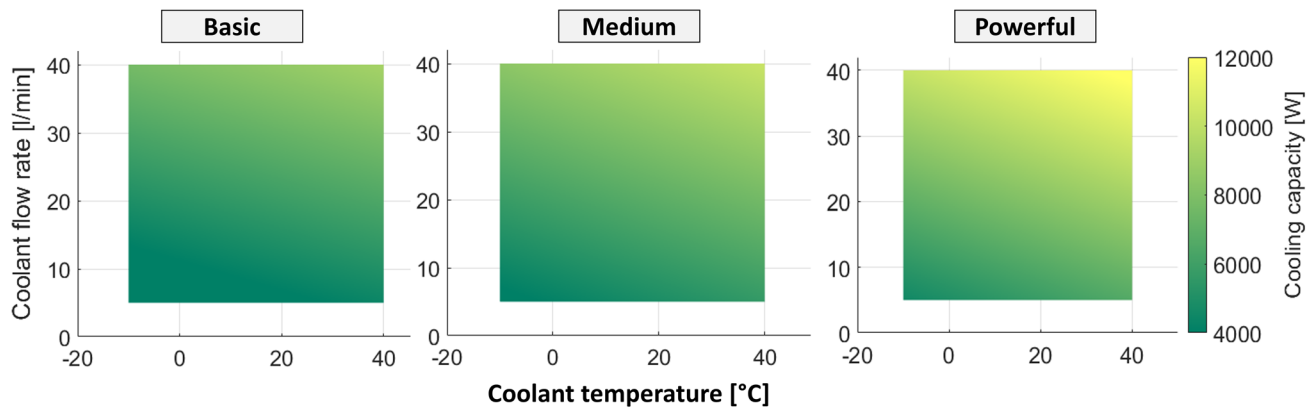
Figure 9. Comparison of three different data-based assumed cooling circuit configurations. Cooling capacities depend on coolant temperature and volume flow rate.

$$T_{\text{fluid,out}} = \frac{\dot{Q}_{\text{poss}}}{\dot{m}_{\text{fluid}} \cdot c_{\text{p}}(T)} + T_{\text{fluid,in}}$$

$$\dot{Q}_{\text{poss}} = \begin{cases} \dot{Q}_{\text{cooling,req}} & \text{if } \dot{Q}_{\text{cooling,max}} \geq \dot{Q}_{\text{cooling,req}} \\ \dot{Q}_{\text{cooling,max}} & \text{if } \dot{Q}_{\text{cooling,max}} < \dot{Q}_{\text{cooling,req}} \end{cases} \tag{28}$$

The system-level volume flow of the coolant is given by a controlled pump with a maximal hydraulic power of 45 W. If the temperature difference between the inlet and outlet in the battery system is above 5 K, the PWM (pulse duration modulation) signal of the pump is increased. If the difference is below, the PWM signal is reduced. The same applies to exceeding the permitted inlet temperature. Thus, the pump control can be used in the overall system optimization to optimize the pressure losses depending on the cooling plate topology. As the resulting volume flow depends on the pressure losses of the system, suitable cooling plate configurations can be derived by user-defined maximum pump power.

2.3. Model Limitations

In this section, the model assumptions and the resulting limitations of the model are discussed. The objective and major advantage of the proposed optimization process is to quickly determine the suitability of the cooling plate topology based on a large set of parameters. In addition, sensitivities of different topology parameters can be discovered. For this reason and to increase the number of optimization degrees of freedom, the following assumptions were made. 1) The battery module is assumed to have a constant homogeneous density and heat capacity. 2) Double-sided cooling can be represented by symmetry in height. 3) Only symmetrical cooling plates are considered to scale the modules, according to Figure 6. 4) A simplified refrigeration cycle with a data-based chiller and simplified pressure losses is used.

The framework presented here is used for the initial conception of a cooling plate topology. Here, processes that significantly influence the density or the heat capacity (e.g., the thermal runaway) are not considered. Therefore, constant component-dependent values are determined for the density and the heat

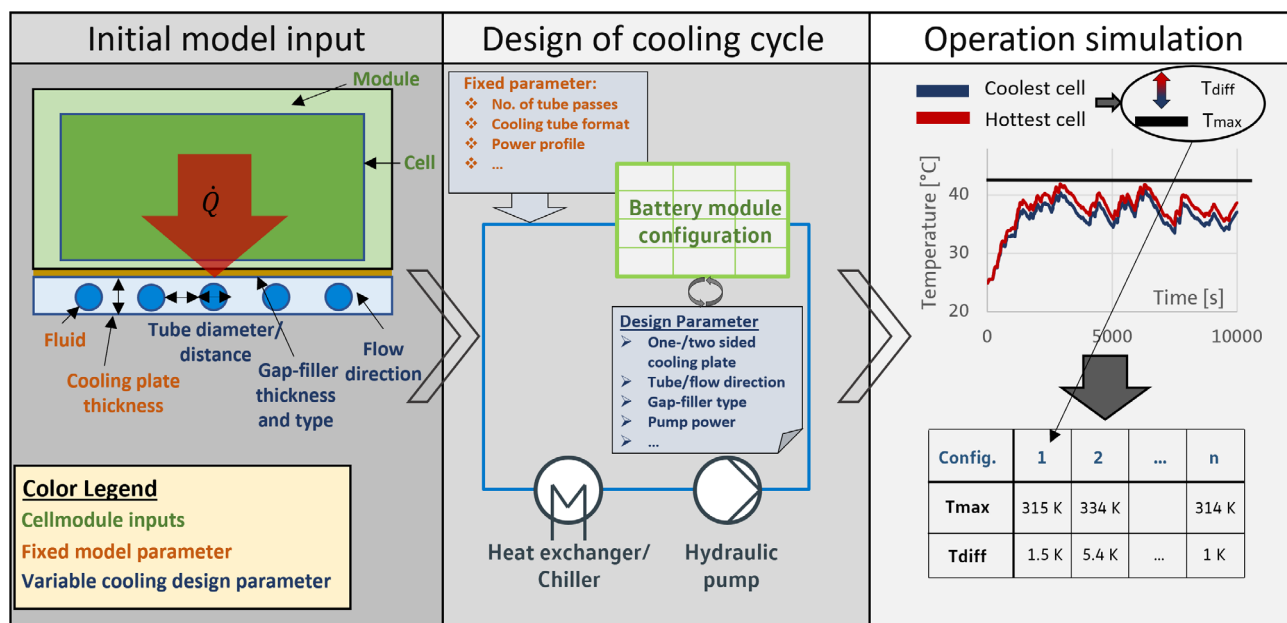capacity. It is assumed that these do not change significantly in the considered temperature range.

This framework is unsuitable for observing and evaluating asymmetries in the cooling plate, which result, for example, from nonequally distributed cooling channels. For this purpose, models with a higher discretization are required. However, higher discretization models cannot ensure fast evaluation of multiple different parameters and are thus unsuitable for higher-level cooling plate topology optimizations.

Using a suitable simplified cooling circuit, the dependencies between fluid temperature, pressure drop, and maximum transferable heat in the chiller are represented in a data-based manner. With these simplifications, the variables from CFD simulations could be mapped with sufficient accuracy. In addition, further conceptual cooling circuits can be mapped with little effort, which is one of the main advantages of the modular approach of the proposed framework. Physics-based modeling of the cooling circuit would significantly increase the complexity and, thus, the computation time, which is why the physics-based modeling approach was not used here. In addition, the cooling circuit is not the focus of this work; different models are required for the detailed design of cooling circuits.

In summary, this framework does not replace a detailed design. However, sensitivities and dependencies can be shown. Thus, this framework is suitable for evaluating conceptual states of cooling topologies.

2.4. Model Summary, Usage, and Optimization Procedure

The proposed cooling plate optimization model can be used to analyze the cooling capability of different cooling plate topologies based on numerous physical EV battery requirements. The framework evaluates the entire battery cooling process from the cellmodules to the cooling plate to the cooling circuit. A three-step workflow is used to evaluate the plate topologies with the abovedescribed models. **Figure 10** depicts these three steps schematically and also shows the major inputs, parameters, and outputs of the optimization framework. An extended list of all input and output parameters is given in the Appendix (see **Table A1** and **Table A2**).

ADVANCED
SCIENCE NEWS
www.advancedsciencenews.com

Energy Technology
Generation, Conversion, Storage, Distribution

www.entechnol.de

Figure 10. Three-part workflow of the cooling plate optimization model to evaluate different cooling plate topologies. First: determination of the initial inputs for the cellmodules and constraints for the cooling plate. Second: cooling cycle design by defining fixed parameters and setting changeable design parameters. Third: evaluation of each cooling plate configuration based on resulting temperatures. Adapted with permission.[60] Copyright 2022, Elsevier.

As the first step, the chosen cellmodules has to be electrically, thermally, and geometrically described and parameterized as the model's major input parameter (see Section 2.1).

In the second step, the boundary conditions for the cooling circuit and plate are defined. Fixed model parameters (current profile, cooling chiller expansion stage, circular shape of cooling tube) are first specified. Additionally, variable cooling design parameters can be optionally set depending on the type of study. These include, for example, the thickness and type of gap filler, the direction of the cooling channels, or the maximum PWM of the water pump (see Section 2.2).

In the last step, the results of the different parameter variations (e.g., cooling tube diameters and tube-to-tube distances) can be evaluated. Different temperatures (maximum, average, max. difference) can thus be directly compared for the different cooling plate configurations. Since all other model parameters are fixed throughout the optimization, resulting temperature changes can be related directly to the changed parameter variations. Afterward, Pareto-optimal design-relevant results can be derived. The model's runtime for optimizing the cooling tube diameter given one cellmodules geometry measures roughly 40–50 s on a standard office notebook with an Intel(R) Core(TM) i5-10310U and 8 GB of RAM.

3. Results and Discussion

When designing a cooling plate for a battery system, the individual cooling plate tube topology must be optimized to efficiently cool the cellmodules with the included cells. Depending on the construction method used, the distances (tube to tube) between the cooling channels cannot be chosen arbitrarily. In addition,

the size of the cooling tubes must be defined depending on the tube-to-tube distance. The size of the cooling tubes also influences the cooling capacity via the heat transfer area, the pressure losses, and the resulting volume flow. In this section, the above-described model will be used to optimally design the cooling plate for an exemplary battery pack with specific requirements and with differing cellmodules geometry possibilities. Thus, three geometrically different cellmodules are prior defined, stressing the applicability of the multiparametric cooling plate simulation model. The geometric input properties of the cooling plate and the cellmodules can be found in **Table 2**.

Figure 11 describes the derivation of the observed cellmodules geometries from the same EV battery pack. The battery pack space allows the cellmodules to be at various geometries. The three cellmodules are divided geometrically into their naming pattern: long, medium, and quadratic. However, the electrical and thermal properties of all cellmodules are kept equal. Table 2 additionally provides a detailed physical description of the cellmodules and cooling plate as well as fundamental cooling model input specifications. The specifications are based on assumed values for a midrange vehicle and thus provide a holistic standard for a cooling plate and its cooling circuit.

Generally, various load profiles can be used as cooling plate design profiles. However, for the analyses in this work, a 25-minute constant current quick charging profile from 5% to 75% SOC was defined (see current profile in Figure A1 in the Appendix). The high current generally ensures maximum cooling capacity from the cooling system in a short duration and is, therefore, particularly relevant for the cooling plate design in today's automotive battery development. In comparison, a 25 min battery charge from 5% to 75% is a moderate-to-high quick charging time for modern EVs. Based on the maximum pump power

ADVANCED
SCIENCE NEWS
www.advancedsciencenews.com

Energy Technology
Generation, Conversion, Storage, Distribution

www.entechnol.de

Table 2. Physical description of evaluated cellmodules and corresponding cooling model specifications.

Specification	Model input parameter	Model assumption
Cooling model	
Used cooling circuit stage	'Basic' (derivation in Figure 9)
PWM pump power	PWM 30%
Cooling plate geometry and material properties	Two-part cooling plate (e.g., soldered together) made of aluminum consisting of an upper base plate (2 mm) and a lower plate (1 mm) with deep drawn cooling channels (variable height).
Cooling plate	One-sided bottom cooling
Cooling design current profile and starting cell SOC	Quick charging protocol (constant current) for 25 min charge from 5% to 75% SOC (see the visualization in Figure A1 in the Appendix)
Cooling tube circle ratio	$w/h = 3$ (derivation and visualization in Figure 5)
Gap filler (thickness and heat conductivity)	Gap filler thickness (cooling plate to cellmodules): 1 mm
	Heat conductivity: 2 W $(m^{-2}\,K^{-1})$
Cooling tube direction	Parallel through the cellstacks (see Figure 11)
Number of passes for each tube	$2 \to$ u-shape tube, see Figure 6
Battery model	
System level data	
Overall size of the cooling plate	$1580 \times 755 \times 18$ mm^3 (optimized height can vary with tube size)
Battery system energy	≈ 51 kWh
Battery system topology	192s1p
Number of modules	8
Module level data	
Module size (length, width, height)	Long: $1440 \times 90 \times 120$ mm^3
	Medium: $720 \times 180 \times 120$ mm^3
	Quadratic: $360 \times 360 \times 120$ mm^3
Module topology	24 total cells; 24s1p interconnection
Module heat capacity	1060 J $(kg\,K)^{-1}$; Module weight 31.1 kg (including 24 cells and aluminum housing shell)
Module heat conductivity (x,y,z)	Along module (side to side): 30 W $(m^{-2}\,K^{-1})$
	Along module (bottom to top): 14 W $(m^{-2}\,K^{-1})$
	Through module (front to back): 1 W $(m^{-2}\,K^{-1})$
Cell level data (see also Appendix)	
Cell properties	Cell format: Pouch-Type
	Cell capacity: $C_{cell} = 72$ Ah
	Cell voltage: $U_{nom} = 3.7$ V
	(Voltage and resistance data tables in the Appendix provide more information)
Busbar	Tab geometry (length, height, thickness): $40 \times 30 \times 0.3$ mm^3
	Busbar (aluminum) geometry cell to cell (length, height, thickness): $36 \times 30 \times 3$ mm^3

(see Section 2.2.5), a PWM signal of 30% is assumed for the following results. Since the battery system is rather small, with

roughly 51 kWh (see Table 2), it can be assumed that also a rather small water pump would be used for the battery cooling system. The sensitivity of the PWM signal will be further discussed to elaborate on the model's robustness in Section 3.3.

Additionally, Figure 11 gives insights into the design possibilities of cooling plates using different cooling tube sizes as well as varying tube-to-tube distances. Based on this, Section 3.1 will introduce the graphical output scheme to examine and evaluate the differently designed cooling plates. Afterward, a variety of different cooling plate topologies will be investigated and evaluated in detail using the module medium geometry. Thereby, different evaluation sizes will be examined to then highlight and discuss the results from various perspectives.

In Section 3.2, the cooling plate topology evaluations are also carried out for the other module geometries long and quadratic.

Section 3.3 will summarize, compare, and discuss the results from an overall view.

## 3.1. Result Evaluation of Module Geometry Medium

In this section, results for the module medium geometry are evaluated and discussed. Unless otherwise described, the assumptions from Table 2 apply. As a first step, results for the mean module temperature for a fixed tube-to-tube distance of 21 mm are depicted in **Figure 12**. This limits the parameter variation of the cooling plate to one only parameter, the cooling channel height. The following analyses assume that the width of the cooling tubes equals three times the tube's height. This was defined in Table 2 (see also the definition of the circular tube segments in Section 2.2.2). The average module temperature (y-axis) is depicted for different cooling tube heights (x-axis), resulting from fast charging the defined battery module. Using the mean module temperature as the major evaluation variable offers advantages in comparing the total heat that can be dissipated depending on the cooling configuration. For an actual feasibility evaluation of a cooling topology, further quantities like the occurring maximum temperature and the maximum occurring temperature difference should be investigated. However, the absolute values of these quantities strongly depend on the current profile and the internal resistances of the cellmodules and can thus change application dependent. Therefore, the mean module temperature is the most suitable parameter for the comparison of cooling plate configurations for a constant module geometry.

The results of the mean temperature depending on tube height show a three-part degressive course. The mean temperatures lie in a range from ≈ 46 to 50 °C. In order to explain the three-part range, the number of tubes fitting underneath the module is represented by different symbols in the graph. Each tube has two passes (see Table 2). The jumps between these tube number clusters are significant at ≈ 1.5 and 2.2 °C. The degressive course results from the increasing pressure losses due to smaller cooling channel diameters. This effect will be discussed in more detail below. Due to the degressive course, the best cooling result is achieved with a tube height of roughly 3 mm.

However, this result is only evaluated as optimal for the considered tube-to-tube distance of 21 mm. In the following, this
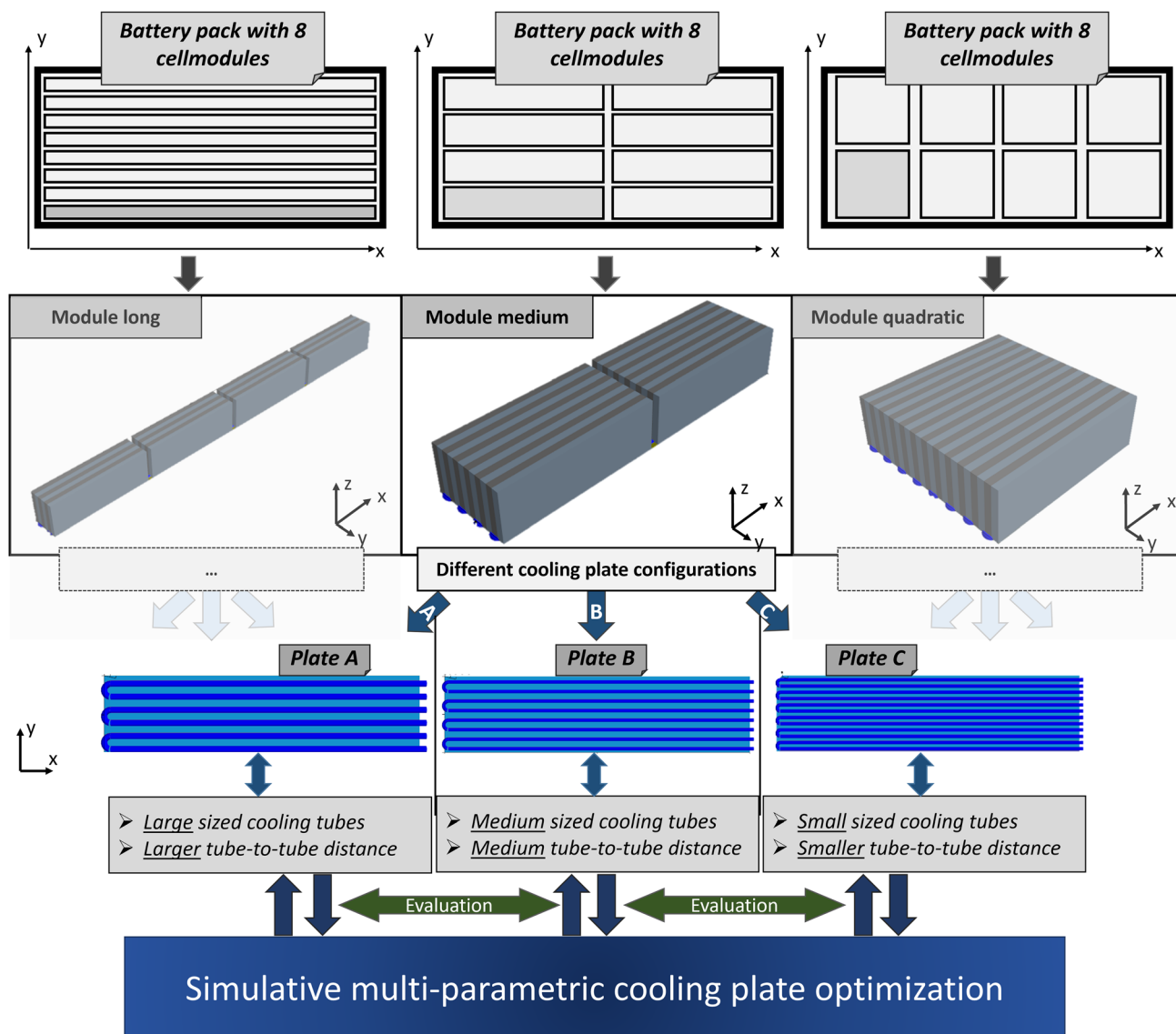
Figure 11. Derivation of the three geometrically different battery cellmodules. The cellmodules's cooling plates are optimized in terms of tube sizes and tube-to-tube distance.
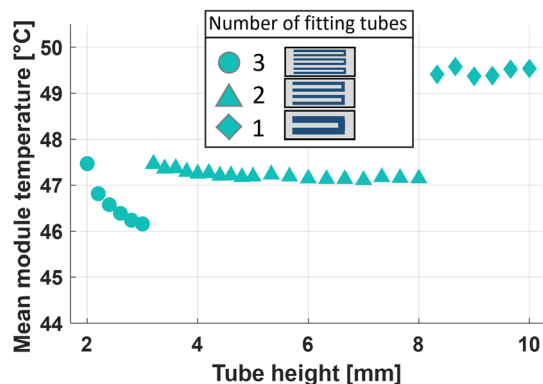
Figure 12. Resulting mean cellmodules temperature for 25 min quick charging with parallel cooling tube flow and a fixed tube-to-tube distance of 21 mm. Different tube heights influence the reached mean module temperature.

premise is removed, and a range of tube-to-tube distances from 11 to 25 mm is investigated. **Figure 13** analyzes these results from different perspectives. The figure is divided into four individual graphs.

Figure 13A shows the resulting reached mean temperatures (y-axis) within the module medium geometry depending on the cooling tube height (x-axis). The color of the data points provides information regarding the evaluated tube-to-tube diameter (11 mm in blue to 25 mm in yellow). As already shown in Figure 12, degressive mean module temperature curves with jumps can be evaluated. These result from the number of geometrically suitable cooling tubes underneath the module geometry given the corresponding tube-to-tube distance as well as the size of the cooling tube. The size of the mapped data points varies slightly with the associated tube-to-tube distance. This ensures that data points with different tube-to-tube distances can visually lie on top of each other. The direct superposition of data points
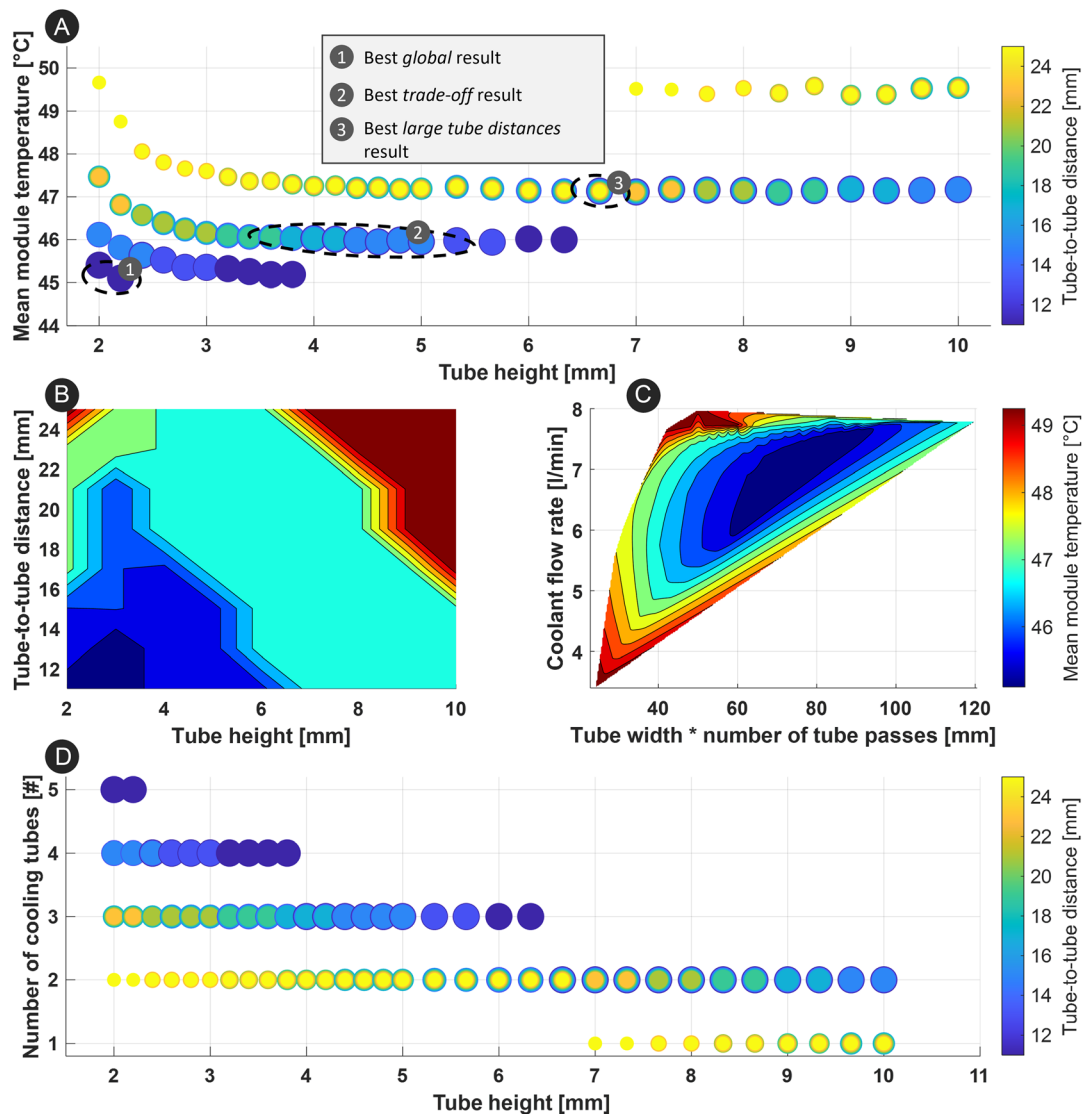
Figure 13. A) Resulting mean cellmodules temperature for 25 min quick charging with parallel cooling tube flow and variable tube-to-tube distance. Different tube heights and tube-to-tube distances influence the reached mean module temperature. B) In-depth view of the mean temperature areas for different geometric cooling tube configurations. C) Volume flow analysis depending on the heat transfer surface. D) Geometric derivation of the number of total fitting cooling tubes depending on the configuration parameters' tube height and tube-to-tube distance.

results from the modeling methodology and geometry assumptions described in Section 2.2.

Figure 13B shows the dependence of the tube height (x-axis) and tube-to-tube distance (y-axis) with the achieved mean module temperature in a 2D contour plot. The color scale from blue to red provides information on the reached mean module temperature. Lower temperatures are achieved with smaller tube diameters or smaller tube-to-tube distances.

Figure 13C can be used to investigate the dependence of system coolant flow rate (y-axis), heat transfer area (x-axis), and mean module temperature (color). The heat transfer area is obtained by multiplying the width of the cooling channels by the number of tubes underneath the cellmodules. It should be noted that the heat transfer area depends on both the tube-to-tube distance and the size of the cooling tubes. A specific value can

thus be obtained from different combinations of the two quantities, which explains the range of associated coolant flow rates in some values of the x-axis. The graphic underlines the complexity of the relationship between the heat transfer area and reached module temperature.

Figure 13D shows the geometrically suitable cooling tubes (y-axis) underneath the module geometry, given the corresponding tube height (x-axis) and tube-to-tube distance (color). The graph can be used to in depth study the depicted results of graphics A–C.

The results can be evaluated on the basis of different quantities or perspectives. Therefore, three result perspective areas have been marked separately in Figure 13A. The first area is the globally optimal result, which can be found in the lower left corner at small tube heights and smaller tube-to-tube distances.

Here the lowest mean module temperatures are achieved. Since the producibility of several very small cooling channels can be complex, the best trade-off result marked with number 2 could also be application dependent optimal. The range is intended to cover a selection of points between which the optimal combination of tube height and tube-to-tube distance is mapped, depending on the manufacturability and the production technology of the cooling plate. The mean module temperatures are roughly 1 °C higher at ≈46 °C. A third range has been marked to derive the best result with the maximum tube-to-tube distance. For cooling plate production using deep-drawing technology, the tube-to-tube distance parameter can be particularly relevant due to producibility-related boundaries and must therefore be carefully selected for some applications. The mean module temperature for the third area is roughly 47 °C.

Assisting the results of the three perspective areas, Figure 13C illustrates generally lower mean module temperatures for medium-to-large heat transfer areas and coolant flow rates. However, the red surface in the upper left part of the graphic is particularly striking. Herein, comparatively high mean module temperatures are achieved despite a high coolant volume flow. This effect can be explained by considering the combination of a few large-sized cooling tubes. Thereby, a generally high coolant volume flow is achieved due to advantageous pressure losses in larger cooling tubes. However, the combination of only a few tubes leads to a nonsufficient cooled cellmodules. Generally, the

results in Figure 13C underline the complexity of optimized cooling tube selection as high volume flows or heat transfer areas do not fully indicate the lowest mean module temperatures.

3.2. Results for Module Geometry: Long and Quadratic

In this section, results for the module long and quadratic geometry are evaluated and discussed. Unless otherwise described, the assumptions from Table 2 apply. The two module geometries long and quadratic, considered here, are shown graphically in Figure 11. Both module geometries do not differ in their physical properties (except geometrically) from the module medium geometry evaluated in the last section. The changed cell arrangement and different space allocation resulting from the associated module geometry majorly change the demands for the optimized cooling plate. **Figure 14** summarizes the results for both geometries. Thereby, Figure 14A again shows different mean temperatures achieved for the cellmodules long geometry. The mean module temperature (y-axis) is depicted depending on the cooling tube height (x-axis) for different tube-to-tube distances (color). Figure 14B shows the associated coolant flow rate instead of the mean temperature on the y-axis. Figure 14C,D are built in the same way and shows the results for the quadratic geometry modules.

The results in Figure 14A,C are again evaluated with respect to three different perspectives. The first perspective is the best
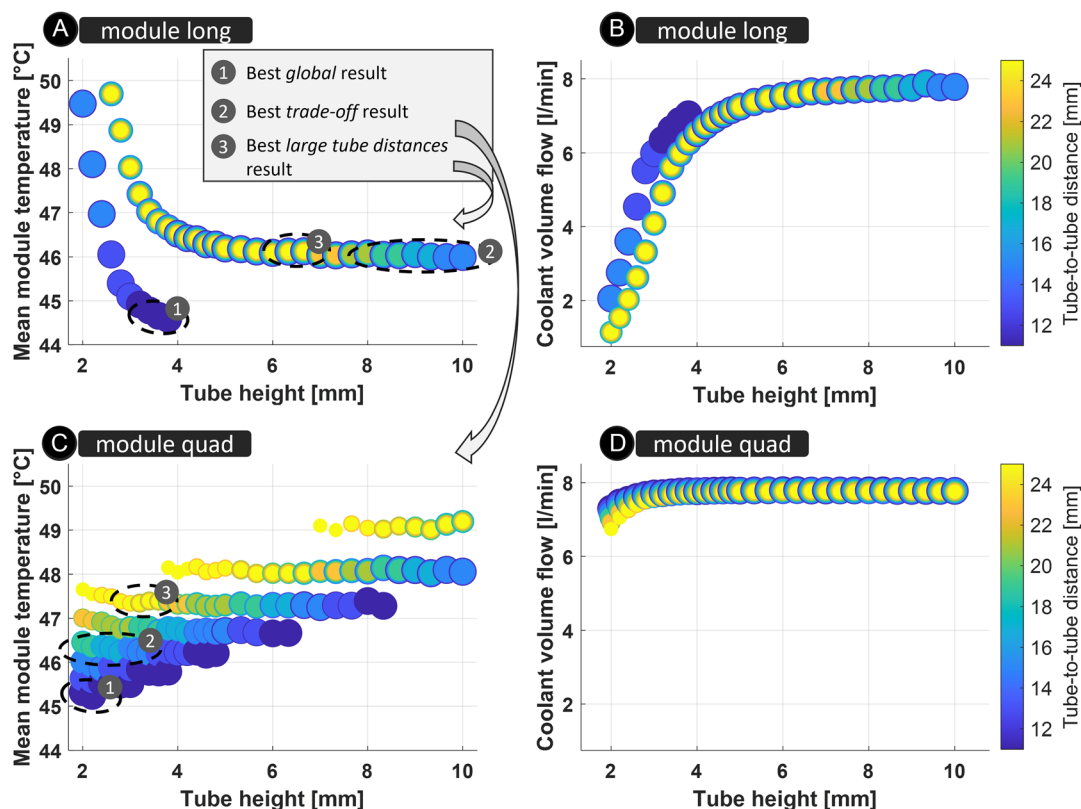
Figure 14. A,C): Resulting mean cellmodules temperature for 25 min quick charging with parallel cooling tube flow and variable tube-to-tube distance. B, D): Volume flow results.

ADVANCED
SCIENCE NEWS

www.advancedsciencenews.com

Energy Technology
Generation, Conversion, Storage, Distribution

www.entechnol.de

global result. The lowest temperature for module long is roughly 44.5 and above 45 °C for module quadratic. While the best global result for the module quadratic can be found at very small tube heights with also small tube-to-tube diameters, the global best result for the module long variant is at about 4 mm tube height. The reason for this lies in the geometry of the module long. Due to the necessary longer cooling tubes, generally, high-pressure losses occur. Therefore, a globally optimal result requires a higher tube height in order to keep the pressure losses small and thus increase the volume flow. This phenomenon can be in detail analyzed in the corresponding Figure 14B,D. Herein, it can be seen that the coolant volume flow for the module quadratic is above 7 L min^{-1} for every evaluated tube height, while for the module, long, larger tube heights are required to increase the volume flow and thus the heat that can be dissipated.

This trend can also be seen in the evaluation by the other evaluated perspectives. The best trade-off result (2) for the module-long variant shows a wide range with larger tube heights, while lower tube heights are needed for the quadratic module. Similar results are evaluated for the result with the largest tube-to-tube distance.

In summary, the module-long variant requires significantly greater tube heights than the module quadratic geometry. This results, in particular, from the pressure losses occurring from the long cooling tubes required in the module-long geometry.

3.3. Summary and Discussion

The optimization methodology developed in this work has allowed a variety of different cooling plate configurations to be investigated and evaluated. The results shown above have provided an overview of the evaluation possibilities with varying tube height and tube-to-tube distance for three different cellmodules geometries.

The different pressure losses, as well as corresponding coolant volume flow rates, resulted in degressive decreasing mean cellmodules temperatures depending especially on the cooling tube's height. This degressivity is directly related to the required length of the cooling channels. Therefore, the degressive course was particularly strong for module long but almost not recognizable for module quadratic.

For each of the investigated module geometries, results were clustered. Through the different clustering criteria (best global, best trade-off, best with maximized tube-to-tube-distance), individual cooling plate configurations were perspective related and evaluated better or worse. In-detail investigations of the module medium geometry underlined the model depth, thus, emphasizing the interaction between the geometrical quantities of tube height and tube-to-tube distance, as well as the necessary volume flow and the achieved mean module temperature.

3.3.1. PWM Signal Robustness

One relevant assumption made for the above-shown results was the pump power using the PWM signal in Table 2. The pump power was initially defined based on the rather small battery system size. However, in a real-world application, the actual pump

size within the battery cooling system may depend on multiple other factors (cost, pressure losses outside the cooling plate, and coolant). Analyzing different PWM signals, thus, investigates the opportunities for larger or smaller dimensioning of the pump used in the final battery cooling system. In order to validate the robustness of the result, the PWM signal was varied, observing again the module medium temperatures. **Figure 15** summarizes these results.

The circle in gray color represents the results of the default pump assumptions from Figure 13. The squares represent results using a PWM signal of 50% with respect to the maximum pump power (see Section 2.2.5). The triangles correspond to the temperature results with a 20% PWM signal.

The results show that the mean temperature course remains largely the same with respect to the tube height and tube-to-tube distance. As expected, an increased PWM signal reduces the average temperature, while a lower PWM signal increases the mean module temperature. The explanation can be found in the increase or decrease of the resulting volume flow corresponding to the pump power. The resulting clustering (best global, best trade-off, best large tube distance) is almost not changing by the varied PWM signal. Only the best global result for the 20% PWM results is shifted toward larger tube heights of almost 4 mm.
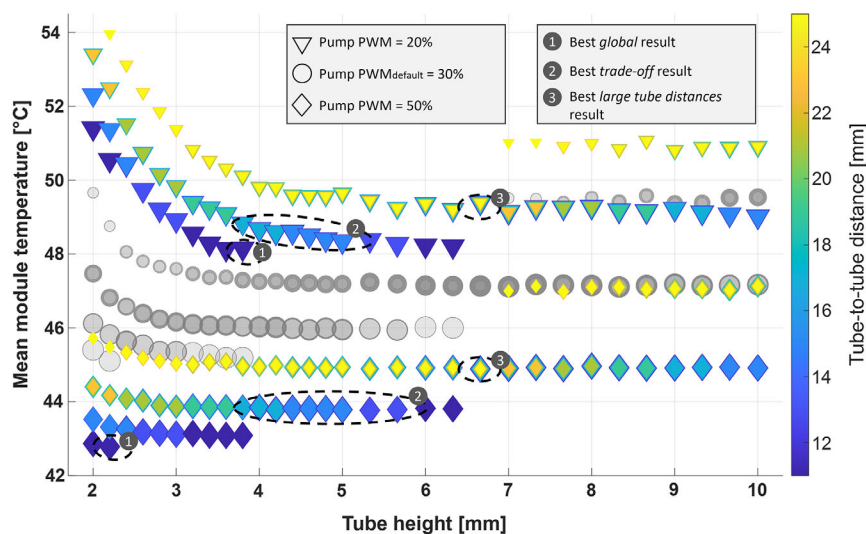
Larger changes can, however, be observed in the initial degressive drop in mean module temperature, especially at smaller tube heights. With a higher PWM signal, the temperature drop becomes less degressive. This could make smaller tube heights more attractive for the cooling plate design, as stronger pumps offer sufficient power for an increased volume flow even for more considerable pressure losses. In conclusion, the pump strength showed no significant influence on the distribution and shape of the results but had relevance in the detailed cooling plate design and especially the interpretation and conclusion of the results. Future work could further elaborate on this aspect and especially investigate it for the different module geometries.

3.3.2. Overall Comparison

A comparative and summarizing analysis between the module geometries considered in this work is depicted in **Figure 16**. The graphic depicts the collectively calculated mean module temperature for each module geometry with the default assumptions from Table 2. Thereby, module long shows the lowest mean module temperatures, followed by module medium and module quadratic. Nevertheless, the highest temperature reached is also achieved by module long, followed by module medium, and module quadratic. A low tube-to-tube distance leads to the greatest advantages within the module-long geometry. This results in an optimal trade-off between heat transfer surface (4 mm tube height), high volume flow (>7 L min^{-1}), and high homogeneity (low tube-to-tube distance), which leads to an overall optimal cooling plate configuration due to the long-shaped geometry.

4. Conclusion

A comparative evaluation of various cooling plate designs was performed, analyzing the potential of different construction-relevant plate properties based on realistic EV battery

**ADVANCED
SCIENCE NEWS**

www.advancedsciencenews.com

Energy Technology
Generation, Conversion, Storage, Distribution

www.entechnol.de

Figure 15. Comparison of three different PWM pump powers. Resulting mean cellmodules temperature for 25 min quick charging with parallel cooling tube flow and variable tube-to-tube distance. Gray dots replicate results from Figure 13 for a graphical comparison.
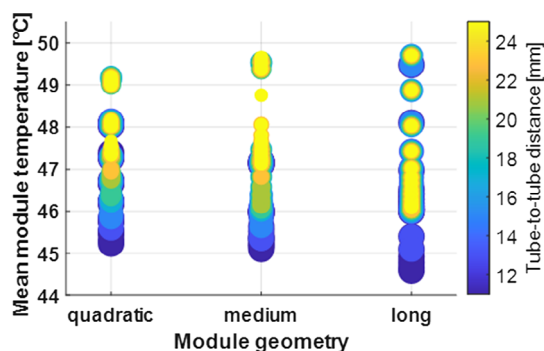
Figure 16. Comparison of all three different module geometries with varying tube-to-tube distances. Range of mean cellmodules temperature reached for 25 min quick charging protocol.

requirements. The proposed cooling plate optimization model is fully parametrized using multiple individual submodels to present the entire battery cooling procedure from the cellmodules to the cooling plate to the cooling circuit. The model incorporates geometric limitations, occurring pressure losses, and operating point-specific cooling capacity.

Three exemplary cellmodules were derived from an EV battery pack to examine the cooling plate optimization model. Based on the cellmodules geometries, various unique simulations with multiple tube diameters as well as tube-to-tube distances were conducted and analyzed. The results mainly emphasized these points. 1) Optimized cooling plate topologies majorly differ depending on the cellmodules geometry: The three cellmodules were defined with equal electrical and thermal but different geometric properties. The results showed the smallest optimized cooling plate tube diameters for the quadratic module (2 mm height) and the largest tubes for the narrow module long

(4 mm height) 2) the lowest mean temperature for the narrow cellmodules long geometry: The module-long variant showed an optimal trade-off between heat transfer surface, high volume flow, and high homogeneity. For otherwise equal conditions, the cooling plate of the module long could thus reach up to 1 °C lower average temperatures for a 25 min constant current quick charging profile.

Different evaluation criteria helped to evaluate results from different perspectives and ultimately elaborate production-specific requirements for developing the cooling plate. Next to module temperatures, also heat transfer areas, resulting volume flows were extracted from the results to stress the model's accuracy and highlight specific cooling configurations. The main findings are as follows. 1) Analysis of trade-offs in cooling plate design using the proposed lumped mass model: The proposed lumped mass model was used to visually emphasize the complex trade-off between coolant volume flow and heat transfer area for multiple cooling plate topologies. The results suggested that only a simultaneous increase in both quantities can lead to an effective temperature decrease. 2) Possibility of potential identification in early concept development phase: Results show the potential of lumped mass modeling to evaluate cooling plate topologies for early-stage concept development stages of EV batteries. Thereby, the preselection of potential cooling plates can give a competitive starting point for the subsequent cooling plate concept with more detailed CAD models. 3) Future-proof modeling approach: The model is built modular and fully parameterized. The generically modeled individual submodels (pressure losses, cooling circuit, plate parametrization) of the cooling model use state-of-the-art data assumptions. Models can be changed, replaced, or extracted to be used in future cooling plate developments. Thereby future work can examine further related cooling methods, such as refrigerant cooling, or novel approaches like immersion cooling, using the proposed model framework.

Appendix

A1. Normalized Reference Cell Data

Normalized reference cell data for a typical automotive NMC-Type battery cell.

A1.1. Voltage Data

The values below are factors related to the $U_{charge,ref}$.(Table A3).

A1.2. Charge Resistance Data

A1.2.1. Rint Data

The values below are factors related to the $R_{charge,ref}$. (Table A4).

A1.2.2. 2-RC Model Charge Resistance Data

Ro Element

The values below are factors related to the $R_{charge,R0,ref}$. (Table A5).

R1 Element

The values below are factors related to the $R_{charge,R1,ref}$. (Table A6).

τ_{R1} Element

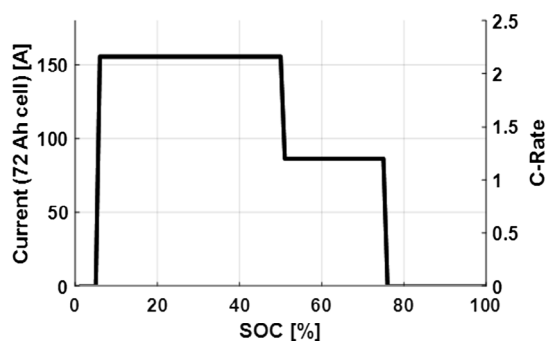The values below are factors related to the $\tau_{charge,R1,ref}$. (Table A7).

Figure A1. Quick charging protocol for 25 min 5–75% SOC charge.

Table A1. Main model input parameters and explanation.

General model input parameter	Explanation
Ambient temperature	Assumption for the evaluation of heat transfers to ambient temperature
Heat transfer coefficient	heat transfer coefficient = 5 W/m²K
Charge/Discharge profile	Cooling plate design profile (driving profile or fast charging profile).
Tube heights	List of possible cooling tube heights. (Parameter is optimized in this study.)
Used cooling circuit	Selected refrigeration circuit (Basic, Medium, Powerful).
Pump power	PWM signal indicating the available power of the coolant pump.
Number of passes	Number of assumed passes for each cooling channel.
Flow direction	Cooling channel direction (parallel or perpendicular to the battery cells). (Parameter is set as parallel in this study.)
Temperature difference for inlet and return temperature of coolant (deltaTmax coolant)	Maximum temperature difference between inlet ($T_{fluid,in}$) and return temperature ($T_{fluid,out}$) of the coolant. See details and control in Section 2.2.5. Default control to 5 K.
Tube-to-tube distance	Geometric distance between two cooling tubes. (Parameter is optimized in this study.)
Gap filler thickness	Thickness of assumed gap filler between the cellmodules and cooling plate.
Gap filler types	List of possible heat conductivity of the assumed gap filler. Parameter can be optimized.
cellmodules specifications	cellmodules geometries
	Number of cells
	cellmodules topology (interconnection 'x's'y'p)
	Stacking direction
	Thermal data (heat capacity, heat conductivity)
	Cell voltage, resistance, capacity
	Busbar model

Table A2. Main model output parameters and explanation.

Output parameters	Explanation
cellmodules parameters	
T_{max}	Maximum temperature reached within the cellmodule.
T_{mean}	Average temperature reached within the cellmodule.
deltaT_{max}	Maximum temperature difference within the cellmodule.
Cooling circuit parameters	
Coolant volume flow	Required flow rate to meet the deltaTmax coolant requirement (for a given PWM signal).
PWM coolant pump power	Required pump capacity to achieve the required volume flow rate (for a given volume flow, depending on the cooling plate topology and resulting pressure losses).
Cooling plate construction parameter	
Mass, costs	Mass and cost estimation of cooling plate configuration.
Optimized cooling plate configuration	Optimized cooling plate configuration includes: 1) One or two-sided cooling and total thickness of the cooling plate; 2) Cooling tube design (construction-based): Height, width and tube-to-tube distance (Parameter is optimized in this study.); 3) heat conductivity and thickness of gap filler; and 4) Reached cellmodules temperatures (max., mean, delta) for the prior defined load profile

Table A3. Reference OCV data.

SOC/Temp	−25 °C	−10 °C	0 °C	10 °C	25 °C	40 °C
0	0.77	0.80	0.81	0.81	0.81	0.80
0.05	0.84	0.84	0.84	0.84	0.84	0.84
0.1	0.86	0.86	0.85	0.86	0.85	0.85
0.15	0.87	0.87	0.87	0.87	0.87	0.87
0.2	0.88	0.88	0.88	0.88	0.88	0.88
0.25	0.89	0.89	0.89	0.89	0.89	0.89
0.3	0.90	0.90	0.90	0.90	0.90	0.90
0.35	0.90	0.90	0.90	0.90	0.90	0.90
0.4	0.91	0.91	0.91	0.91	0.91	0.91
0.45	0.92	0.92	0.92	0.92	0.92	0.92
0.5	0.93	0.93	0.93	0.93	0.93	0.93
0.55	0.94	0.94	0.94	0.94	0.94	0.94
0.6	0.95	0.96	0.96	0.96	0.96	0.96
0.65	0.96	0.97	0.97	0.97	0.97	0.97
0.7	0.98	0.98	0.98	0.98	0.98	0.98
0.75	0.99	0.99	0.99	0.99	0.99	0.99
0.8	1.00	1.00	1.00	1.00	$U_{charge,ref}$	1.00
0.85	1.01	1.01	1.01	1.01	1.01	1.01
0.9	1.02	1.02	1.02	1.02	1.02	1.02
0.95	1.03	1.03	1.03	1.03	1.03	1.03
1	1.04	1.04	1.04	1.04	1.04	1.04

Table A4. Reference Rint charge data.

SOC/Temp	−25 °C	−10 °C	0 °C	10 °C	23 °C	40 °C
0.1	14.90	4.87	2.85	1.89	1.27	0.82
0.2	7.53	2.87	1.71	1.15	0.95	0.82
0.3	5.65	2.60	1.73	1.21	0.92	0.82
0.4	4.63	2.40	1.62	1.14	0.81	0.74
0.5	4.34	2.21	1.47	1.01	0.86	0.72
0.6	4.47	2.53	1.93	1.37	1.22	1.03
0.7	5.42	3.11	2.05	1.68	1.25	1.00
0.8	5.28	2.71	1.69	1.37	$R_{charge,ref}$	0.80
0.9	5.35	2.33	1.41	0.99	0.68	0.52

Table A5. Reference 2RC-model data: R0 element.

SOC/Temp	−25	−10	0	10	23	40
0.1	15.62	5.56	2.80	1.71	1.17	0.92
0.2	10.24	3.81	2.10	1.42	1.05	0.89
0.3	7.65	3.16	1.87	1.32	1.01	0.86
0.4	7.44	2.96	1.78	1.27	0.99	0.85
0.5	7.04	2.85	1.74	1.25	0.98	0.86
0.6	6.88	2.79	1.71	1.23	0.99	0.86
0.7	6.63	2.78	1.72	1.25	1.01	0.87
0.8	6.68	2.82	1.73	1.25	$R_{charge,R0,ref.}$	0.87
0.9	7.58	3.01	1.81	1.28	1.01	0.87

Table A6. Reference 2RC-model data: R1 element.

SOC/Temp	−25 °C	−10 °C	0 °C	10 °C	23 °C	40 °C
0.1	35.43	5.58	3.25	1.65	1.01	0.70
0.2	3.36	2.90	2.18	1.37	0.87	0.59
0.3	3.71	2.87	2.13	1.35	0.87	0.56
0.4	4.31	3.04	2.21	1.39	0.85	0.55
0.5	5.09	3.25	2.30	1.48	0.91	0.57
0.6	5.45	3.46	2.47	1.58	1.01	0.66
0.7	5.32	3.58	2.69	1.46	1.00	0.67
0.8	5.68	3.77	2.69	1.48	$R_{charge,R1,ref.}$	0.66
0.9	6.52	3.55	2.48	1.37	0.92	0.61

R_2 Element

The values below are factors related to the $R_{charge,R2,ref.}$. (**Table A8**).

τ_{R2} Element

The values below are factors related to the $\tau_{charge,R2,ref.}$. (**Table A9** and **Table A10**).

Table A7. Reference 2RC-model data: t1 element.

SOC/Temp	−25 °C	−10 °C	0 °C	10 °C	23 °C	40 °C
0.1	0.83	0.77	1.31	0.99	0.76	0.63
0.2	0.90	1.75	1.46	1.10	0.81	0.66
0.3	0.12	1.86	1.55	1.19	0.89	0.70
0.4	1.78	1.91	1.61	1.26	0.94	0.75
0.5	1.92	1.98	1.66	1.29	0.98	0.81
0.6	1.95	2.03	1.69	1.33	1.05	0.88
0.7	2.18	2.08	1.75	1.28	1.06	0.90
0.8	2.15	2.04	1.68	1.23	$\tau_{charge,R1,ref.}$	0.84
0.9	2.09	1.91	1.53	1.14	0.91	0.77

Table A8. Reference 2RC-model data: R2 element.

SOC/Temp	−25 °C	−10 °C	0 °C	10 °C	23 °C	40 °C
0.1	7.52	4.12	2.76	2.11	1.43	0.79
0.2	6.91	2.16	1.27	0.89	0.91	0.84
0.3	4.81	2.09	1.49	1.07	0.86	0.87
0.4	2.65	1.76	1.29	0.96	0.67	0.73
0.5	2.09	1.39	0.99	0.69	0.74	0.67
0.6	2.35	2.03	1.91	1.40	1.46	1.27
0.7	4.54	3.20	2.08	2.08	1.51	1.21
0.8	4.10	2.28	1.33	1.42	$R_{charge,R2,ref.}$	0.79
0.9	3.29	1.42	0.75	0.66	0.35	0.23

Table A9. Reference 2RC-model data: t2 element.

SOC/Temp	−25 °C	−10 °C	0 °C	10 °C	23 °C	40 °C
0.1	0.62	0.68	0.69	0.60	0.51	0.46
0.2	0.86	0.77	0.75	0.67	0.57	0.52
0.3	0.72	0.88	0.87	0.78	0.69	0.62
0.4	0.88	0.97	0.98	0.93	0.83	0.78
0.5	0.99	1.11	1.14	1.10	1.03	0.98
0.6	1.14	1.26	1.32	1.28	1.17	1.12
0.7	1.40	1.37	1.33	1.22	1.14	1.10
0.8	1.29	1.21	1.14	1.06	$\tau_{charge,R2,ref.}$	0.97
0.9	1.16	1.07	0.98	0.92	0.88	0.86

Table A10. List of abbreviation.

Abbreviation	
AC	Alternating current
BEV	Battery electric vehicle
BTMS	Battery thermal management system
CFD	Computational fluid dynamics
ECM	Electrical equivalent circuit models
EV	Electric vehicle
HV	High voltage
ICE	Internal combustion engine
IEA	International energy agency
LIB	Lithium-ion battery
MSL	Modelica Standard Library
OCV	Open circuit voltage
PWM	Pulse duration modulation
SOC	State of Charge

Symbol	Description	Unit
c_{Rate}	C-rate: Current with respect to nominal capacity	h^{-1}
$\dot{c}_{Rate}$	Time-mean C-rate	h^{-1}
t	Time	s
$\dot{Q}$	Heat flow rate	W
T	Temperature	K
R_{th}	Thermal resistance	KW^{-1}
c_{P}	Specific isobaric heat capacity	$J(kgK)^{-1}$
ρ	Density	$kg(m^{-1})$
V	Volume	m^3
m	Mass	kg
n	Quantity	—
k_{scaled}	Scaling factor for electrical resistance	—
R	Electrical resistance	Ω
I	Current	A
U	Voltage	V
C	Electrical capacitance	F
τ	Time constant	s
$f_{distribution}$	Distribution matrix used for busbar system modeling	—
α	Heat transfer coefficient	$W(m^2K)^{-1}$
Nu	Nusselt number	—
$k_{passive}$	Factor for passive air cooling	—
L	Characteristic length for the fluid flow	m

Table A10. Continued.

λ	Thermal conductivity	$W(mK)^{-1}$
Re	Reynolds number	—
X^+	dimensionless length	—
d	Diameter	m
Pe	Péclet number	—
Pr	Prandtl number	—
l	Tube length	m
ξ	Wall friction coefficient	—
Δp	Pressure drop	Pa
ν	Velocity	ms^{-1}
η	Dynamic viscosity	Pas
$\dot{m}$	Mass flow rate	kgs^{-1}
x, y	Exponents for empirical pressure drop approach	—
k_V	Constant factor for the dependence between transferable heat and volume flow rate in chiller model	$W(m^3s^{-1})^{-1}$
k_T	Constant factor for the dependence between transferable heat and fluid temperature in chiller model	WK^{-1}
$\dot{Q}_0$	Cooling capacity offset in chiller model	W

Superscripts and Subscripts

surface	Surface/Side of discrete element
th	Thermal
module	Related to the module
cell	Related to the cell
M	Material
RC	RC element
Tab, Busbar	Contact of Tab and Busbar
Tab	Tab of battery-cell
Busbar	Busbar in battery module
passive	Passive air cooling
lam	Laminar flow
h	Hydraulic
turb	Turbulent flow
nominal	Related to the nominal conditions
max	Maximum value
cooling	Related to the chiller
fluid	Related to the fluid
req	Requirement
poss	Possible

Acknowledgements

Conflict of Interest

The authors declare no conflict of interest.

Author Contributions

A.E.: Conceptualization, Methodology, Validation, Investigation, Writing the original draft (methods, results and discussion, conclusion), Visualization. S.R.: Conceptualization, Methodology, Writing the original draft (introduction). F.v.G.: Conceptualization, Methodology, Software, Validation, Writing the original draft (methods), Visualization. A.V.: Conceptualization, methodology, software. J.K.: Conceptualization, Supervision. D.U.S.: Conceptualization, Supervision. All authors worked on reviewing and editing.

Data Availability Statement

The data that support the findings of this study are available from the corresponding author upon reasonable request.

Keywords

[1] J. S. Kikstra, Z. R. J. Nicholls, C. J. Smith, J. Lewis, R. D. Lamboll, E. Byers, M. Sandstad, M. Meinshausen, M. J. Gidden, J. Rogelj, E. Kriegler, G. P. Peters, J. S. Fuglestvedt, R. B. Skeie, B. H. Samset, L. Wienpahl, D. P. van Vuuren, K.-I. van der Wijst, A. Al Khourdajie, P. M. Forster, A. Reisinger, R. Schaeffer, K. Riahi, *Geosci. Model Dev.* **2022**, *15*, 9075.

[2] IPCC (Ed.), *Global Warming of 1.5°C: IPCC Special Report on Impacts of Global Warming of 1.5°C above Pre-industrial Levels in Context of Strengthening Response to Climate Change, Sustainable Development, and Efforts to Eradicate Poverty*, Cambridge University Press, Cambridge **2022**.

[3] IEA transport: Improving the Sustainability of Passenger and Freight Transport, https://www.iea.org/topics/transport (accessed: January 2023).

[4] IEA CO2 Emissions in 2022, https://www.iea.org/reports/co2-emissions-in-2022 (accessed: May 2023).

[5] IEA Global EV Outlook 2023, https://www.iea.org/reports/global-ev-outlook-2023 (accessed: May 2023).

[6] S. Ding, R. Li, *Eng. Appl. Artif. Intell.* **2021**, *100*, 104148.

[7] J. Zheng, X. Sun, L. Jia, Y. Zhou, *J. Cleaner Prod.* **2020**, *243*, 118607.

[8] A. Mahmoudzadeh Andwari, A. Pesiridis, S. Rajoo, R. Martinez-Botas, V. Esfahanian, *Renewable Sustainable Energy Rev.* **2017**, *78*, 414.

[9] A. K. Thakur, R. Prabakaran, M. R. Elkadeem, S. W. Sharshir, M. Arıcı, C. Wang, W. Zhao, J.-Y. Hwang, R. Saidur, *J. Energy Storage* **2020**, *32*, 101771.

[10] L. Lu, X. Han, J. Li, J. Hua, M. Ouyang, *J. Power Sources* **2013**, *226*, 272.

[11] M. Armand, P. Axmann, D. Bresser, M. Copley, K. Edström, C. Ekberg, D. Guyomard, B. Lestriez, P. Novák, M. Petranikova, W. Porcher, S. Trabesinger, M. Wohlfahrt-Mehrens, H. Zhang, *J. Power Sources* **2020**, *479*, 228708.

[12] A. Tomaszewska, Z. Chu, X. Feng, S. O'Kane, X. Liu, J. Chen, C. Ji, E. Endler, R. Li, L. Liu, Y. Li, S. Zheng, S. Vetterlein, M. Gao, J. Du, M. Parkes, M. Ouyang, M. Marinescu, G. Offer, B. Wu, *eTransportation* **2019**, *1*, 100011.

[13] A. G. Boulanger, A. C. Chu, S. Maxx, D. L. Waltz, *Proc. IEEE* **2011**, *99*, 1116.

[14] D. Howell, S. Boyd, B. Cunningham, S. Gillard, L. Slezak, *Enabling Fast Charging: A Technology Gap Assessment*, U.S. Department of Energy Office of Scientific and Technical Information, Oak Ridge, TN **2017**.

[15] Jacques Philippe Towards a Competitive European Industrial Battery Value Chain for Stationary Applications and E-Mobility, https://www.2zeroemission.eu/wp-content/uploads/2021/05/Batteries-European-Partnership-General-presentation-Philippe-Jacques.pdf (accessed: February 2023).

[16] S. Panchal, V. Pierre, M. Cancian, O. Gross, F. Estefanous, T. Badawy, in *WCX SAE World Congress Experience* (Eds: S. Panchal, V. Pierre, M. Cancian, O. Gross, F. Estefanous, T. Badawy), SAE Internationa, Warrendale, PA; Detroit, MI **2023**.

[17] V. Talele, M. S. Patil, S. Panchal, R. Fraser, M. Fowler, *J. Energy Storage* **2023**, *65*, 107253.

[18] S. Mukane, P. Mane, A. Gaddam, *Mater. Today Proc.* **2021**, *45*, 2690.

[19] R. Braga, A. Mevawalla, S. Gudiyella, S. Panchal, M. Giuliano, G. Nicol, Y. Zheng (**2023**) in *WCX SAE World Congress Experience* (Eds: R. Braga, A. Mevawalla, S. Gudiyella, S. Panchal, M. Giuliano, G. Nicol, Y. Zheng), SAE International, Detroit, MI; Warrendale, PA.

[20] J. Lempert, P. J. Kollmeyer, M. He, M. Haußmann, J. S. Cotton, A. Emadi, *J. Power Sources* **2022**, *550*, 232121.

[21] A. Kumar Thakur, R. Sathyamurthy, R. Velraj, R. Saidur, A. K. Pandey, Z. Ma, P. Singh, S. K. Hazra, S. Wafa Sharshir, R. Prabakaran, S. C. Kim, S. Panchal, H. M. Ali, *Appl. Therm. Eng.* **2023**, *226*, 120303.

[22] X. Li, J. Zhao, J. Yuan, J. Duan, C. Liang, *J. Energy Storage* **2021**, *35*, 102270.

[23] G. Zhao, X. Wang, M. Negnevitsky, H. Zhang, *J. Power Sources* **2021**, *501*, 230001.

[24] L. F. Cabeza, A. Frazzica, M. Chàfer, D. Vérez, V. Palomba, *J. Energy Storage* **2020**, *32*, 101976.

[25] S. Arora, *J. Power Sources* **2018**, *400*, 621.

[26] H. Hopp, *Thermomanagement von Hochleistungsfahrzeug-Traktionsbatterien anhand gekoppelter Simulationsmodelle*, Springer Vieweg, Wiesbaden **2016**.

[27] N. Nieto, L. Díaz, J. Gastelurrutia, F. Blanco, J. C. Ramos, A. Rivas, *J. Power Sources* **2014**, *272*, 291.

[28] Y. Deng, C. Feng, J. E, H. Zhu, J. Chen, M. Wen, H. Yin, *Appl. Therm. Eng.* **2018**, *142*, 10.

[29] Y. Lian, H. Ling, G. Song, Q. Ma, B. He, *Appl. Ther. Eng.* **2023**, *225*, 120138.

[30] J. Smith, R. Singh, M. Hinterberger, M. Mochizuki, *Int. J. Therm. Sci.* **2018**, *134*, 517.

[31] J. Qu, C. Wang, X. Li, H. Wang, *Appl. Therm. Eng.* **2018**, *135*, 1.

[32] A. K. Joshi, D. Dandotiya, C. S. Ramesh, S. Panchal, in *2023 AeroTech* (Eds: A.K. Joshi, D. Dandotiya, C.S. Ramesh, S. Panchal), SAE International, Warrendale, PA; Fort Worth, TX **2023**.

[33] V. G. Choudhari, A. S. Dhoble, S. Panchal, *Int. J. Heat Mass Transfer* **2020**, *163*, 120434.

[34] S. H. Hong, D. S. Jang, S. Park, S. Yun, Y. Kim, *Appl. Therm. Eng.* **2020**, *173*, 115213.

[35] W. Zuo, J. Li, Y. Zhang, Q. Li, *J. Therm. Anal. Calorim* **2023**, *148*, 3689.

[36] D. Li, W. Zuo, Q. Li, G. Zhang, K. Zhou, J. E, *Energy* **2023**, *273*, 127250.

[37] A. Tang, J. Li, L. Lou, C. Shan, X. Yuan, *Appl. Therm. Eng.* **2019**, *159*, 113760.

[38] J. E, D. Han, A. Qiu, H. Zhu, Y. Deng, J. Chen, X. Zhao, W. Zuo, H. Wang, J. Chen, Q. Peng, *Appl. Therm. Eng.* **2018**, *132*, 508.

[39] A. Jarrett, I. Y. Kim, *J. Power Sources* **2011**, *196*, 10359.

[40] J. Li, W. Zuo, J. E, Y. Zhang, Q. Li, K. Sun, K. Zhou, G. Zhang, *Energy* **2022**, *242*, 123039.

[41] W. Zuo, Y. Zhang, J. E, Y. Huang, Q. Li, K. Zhou, G. Zhang, *Energy* **2022**, *261*, 125384.

[42] Y. Zhang, W. Zuo, J. E, J. Li, Q. Li, K. Sun, K. Zhou, G. Zhang, *Energy* **2022**, *248*, 123637.

[43] W. Zuo, Y. Zhang, J. E, J. Li, Q. Li, G. Zhang, *Renewable Energy* **2022**, *192*, 46.

[44] E. Gonzalez-Aguirre, J. Gastelurrutia, M. Suresh Patil, L. del Portillo-Valdes, *J. Electrochem. Soc.* **2021**, *168*, 110523.

[45] N. Wassiliadis, J. Schneider, A. Frank, L. Wildfeuer, X. Lin, A. Jossen, M. Lienkamp, *J. Energy Storage* **2021**, *44*, 103306.

[46] R. Wendland, P. Padberg, W. Tegethoff, J. Köhler, in *27th Aachen Colloquium Automobile and Engine Technology 2018* (Eds: L. Eckstein, S. Pischinger), Institute for Automotive Engineering, RWTH Aachen **2018**, pp. 335–357.

[47] C. Richter, *Proposal of New Object-Oriented Equation-Based Model Libraries for Thermodynamic Systems*, Technische Universität Braunschweig, Braunschweig **2008**.

[48] C. W. Schulze, *A Contribution to Numerically Efficient Modelling of Thermodynamic Systems*, Technische Universität Braunschweig, Braunschweig **2013**.

[49] R. Wendland, *Ein Beitrag zur thermischen Auslegung von Fahrzeug-Batteriesystemen*, Technische Universität Braunschweig, Braunschweig **2021**.

[50] H. D. Baehr, K. Stephan, *Wärme- und Stoffübertragung*, 9th ed., Springer Vieweg Berlin, Berlin, Heidelberg **2016**.

[51] G. Cerbe, G. Wilhelms, *Technische Thermodynamik: Theoretische Grundlagen und praktische Anwendungen*, 15th edn, Carl Hanser Verlag, München **2008**.

[52] L. Cheng, G. Ribatski, J. R. Thome, *Int. J. Heat Mass Transfer* **2008**, *51*, 125.

[53] S. Jeong, E. Cho, H.-K. Kim, in *ASME 3rd Int. Conf. on Microchannels and Minichannels*, Toronto, Ontario, Canada, June 2005 pp. 103–108.

[54] J. Meintschel, D. Schröter, V. Keck, DE102008059955B4, **2010**.

[55] A. C. Benim, S. B. Maddala, *HFF* **2020**, *31*, 1837.

[56] V. Gnielinski, *Int. J. Heat Mass Transfer* **2013**, *63*, 134.

[57] P. Konakov, *A New Correlation for the Friction Coefficient in Smooth Tubes*, 7th ed., Report of the Academic Society for Science of the UDSSR, Moskov **1946**.

[58] D. Taler, *Int. J. Therm. Sci.* **2016**, *105*, 109.

[59] VDI e. V., *VDI Heat Atlas*, 2nd ed., Springer-Verlag Berlin Heidelberg, Berlin **2010**.

[60] A. Epp, R. Wendland, J. Behrendt, R. Gerlach, D. U. Sauer, *J. Energy Storage* **2022**, *52*, 104854.